

THE CHEMICAL HOMOGENEITY OF OPEN CLUSTERS

Jo Bovy

Department of Astronomy and Astrophysics, University of Toronto, 50 St. George Street, Toronto, ON, M5S 3H4, Canada;
bovy@astro.utoronto.ca

ABSTRACT

Determining the level of chemical homogeneity in open clusters is of fundamental importance in the study of the evolution of star-forming clouds and that of the Galactic disk. Yet limiting the initial abundance spread in clusters has been hampered by difficulties in obtaining consistent spectroscopic abundances for different stellar types. Without reference to any specific model of stellar photospheres, a model for a homogeneous cluster is that it forms a one-dimensional sequence, with any differences between members due to variations in stellar mass and observational uncertainties. I present a novel method for investigating the abundance spread in open clusters that tests this one-dimensional hypothesis at the level of observed stellar spectra, rather than constraining homogeneity using derived abundances as traditionally done. Using high-resolution APOGEE spectra for 49 giants in M67, NGC 6819, and NGC 2420 I demonstrate that these spectra form one-dimensional sequences for each cluster. With detailed forward modeling of the spectra and Approximate Bayesian Computation, I derive strong limits on the initial abundance spread of 15 elements: < 0.01 (0.02) dex for C and Fe, $\lesssim 0.015$ (0.03) dex for N, O, Mg, Si, and Ni, $\lesssim 0.02$ (0.03) dex for Al, Ca, and Mn, and $\lesssim 0.03$ (0.05) dex for Na, S, K, Ti, and V (at 68 % and 95 % confidence, respectively). The strong limits on C and O imply that no pollution by massive core-collapse supernovae occurred during star formation in open clusters, which, thus, need to form within $\lesssim 6$ Myr. Further development of this and related techniques will bring the power of differential abundances to stars other than solar twins in large spectroscopic surveys and will help unravel the history of star formation and chemical enrichment in the Milky Way through chemical tagging.

Subject headings: Galaxy: abundances — Galaxy: disk — Galaxy: evolution — Galaxy: formation — Galaxy: fundamental parameters — Galaxy: structure

1. INTRODUCTION

The surface abundances of long-lived stars observed through high-resolution spectroscopy hold the archaeological record of the conditions of their formation. Carefully uncovering this history through analyses of the observed spectroscopic, photometric, and astrometric data has the potential to lead to transformative insights into the nature of star formation, the evolution of massive stars, and the detailed chemical and dynamical evolution of galactic disks. Yet, after many decades of work on the theory of stellar photospheres and orders of magnitude improvements in the quantity, quality, and variety of observed stellar spectra, stellar spectroscopy remains challenging due to incomplete theoretical models and the difficulty of taking into account the many instrumental factors affecting observations. Because of this, abundance uncertainties are still routinely quoted as being “0.1 dex”, a seemingly magic number even though in practice observational setups vary widely.

Measuring stellar abundances for many different elements with uncertainties $\ll 0.1$ dex opens up a wide range of questions to scientific investigation. Stars are believed to form in groups in molecular clouds (e.g., Shu et al. 1987; Lada & Lada 2003), but exactly how the intracloud medium evolves and mixes and how star formation proceeds in such clouds, especially on timescales of a few Myr (McKee & Tan 2002; Feng & Krumholz 2014), is difficult to study observationally because the young clusters are mostly obscured from view. Determining the spread (or tight limits $\ll 0.1$ dex on it) in the abundances of elements produced on short timescales by

Type II supernovae in surviving clusters would provide strong constraints on analytic and numerical work in this area.

Beyond the individual star clusters, stellar abundances of long-lived stars trace the history of star formation, chemical enrichment, and the interstellar medium. If the majority of stars are born in clusters with tens of thousands of members sharing the same initial abundances, we might be able to chemically tag individual star-formation events in the Milky Way by determining abundances for large samples of stars (Freeman & Bland-Hawthorn 2002). If successful, this tagging would provide the chemical and dynamical history of the Milky Way’s disk at a level of detail far surpassing our currently limited, broad-brush picture (e.g., Bland-Hawthorn et al. 2010). To determine whether chemical tagging is possible, three essential questions remain to be answered: (a) What is the level of initial abundance spread in star clusters? (b) Can we measure the variations between the chemical signatures of different clusters to the level determined in (a) in light of observational uncertainties and the effects of stellar evolution on the present-day surface abundances? And (c) do different star-forming clusters have chemical signatures that are sufficiently unique to distinguish each star-forming event, given the “chemical resolution” attained in (b)?

In this paper I present a novel method for addressing question (a) above through observations of the abundance spread in open clusters and use it to determine the most stringent constraints on the chemical homogeneity of open clusters to date. Old open clusters (with ages

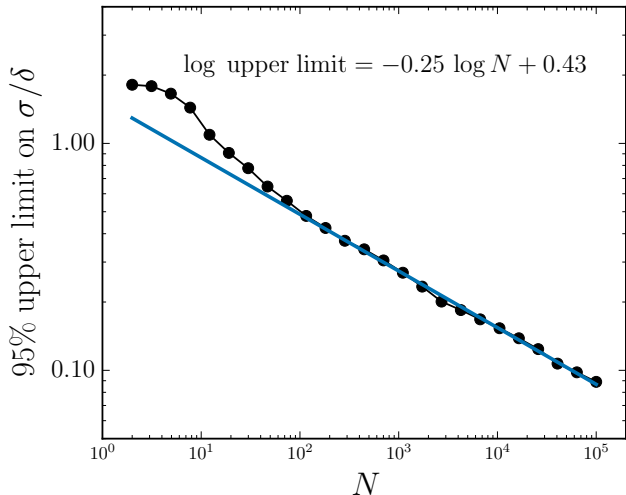


FIG. 1.— The 95 % upper limit on the intrinsic scatter σ for data drawn with uncertainty δ as a function of the number of data points N . Each point corresponds to the median of 50 different mock data sets. The blue line is a fit to the large- N points, with the best-fit parameters indicated in the top right, demonstrating the asymptotic $N^{-1/4}$ dependence of the upper limit on σ/δ derived analytically in the text. For 0.10 dex abundance uncertainties, approximately 100,000 data points would be necessary to limit an open cluster’s intrinsic scatter to below 0.01 dex.

> 1 Gyr) are those rare star-formation remnants that have not been destroyed yet by encounters with molecular clouds. As such, they may constitute a biased sample of the full initial open-cluster population. But it is also likely that an unbiased subset survives the presumably random interactions with gravitational inhomogeneities, in which case they can shed light on the properties of all of the clusters that stars form in.

Previous work has established that open clusters are homogeneous at the level of ≈ 0.05 to 0.1 dex (e.g., De Silva et al. 2006, 2007a,b; Reddy et al. 2012; Ting et al. 2012), although these analyses typically proceed by comparing the observed scatter to the estimated uncertainties, rather than inferring rigorous limits on the scatter. The advent of large surveys of open clusters has allowed such analyses to be performed for many clusters and many different atomic species, with limits on the dispersion now routinely reaching $\lesssim 0.05$ dex (Blanco-Cuaresma et al. 2015). One of the main limiting factors in these studies is the inability to measure abundances on a consistent scale for different stellar types (e.g., dwarfs, sub-giants, giants), reducing the number of stars available for any analysis.

1.1. Limiting intrinsic scatter

Most work on determining or limiting the abundance spread in open clusters does not carefully track the observational uncertainties, even though these are key to establishing whether any measured scatter is real or simply due to measurement errors. To illustrate this, consider a simple experiment where N mock data points d_i with no intrinsic scatter are drawn with Gaussian uncertainties with variance δ^2 . The likelihood for the intrinsic scatter σ when it is assumed to be Gaussian is

$$\mathcal{L}(\sigma) \propto (\delta^2 + \sigma^2)^{-N/2} \exp\left(-\frac{1}{2} \frac{\sum_{i=1}^N d_i^2}{\delta^2 + \sigma^2}\right). \quad (1)$$

This is a χ^2 distribution for the parameter $Q = \frac{\sum_{i=1}^N d_i^2}{\delta^2 + \sigma^2}$ with $N + 2$ degrees of freedom. In the large- N limit, this distribution approaches a Gaussian distribution with

$$x = (Q - N - 2)/\sqrt{2(N + 2)} \sim \mathcal{N}(0, 1), \quad (2)$$

where $\mathcal{N}(0, 1)$ is the unit normal distribution. An upper limit σ_{ul} on σ at some confidence level corresponds to a lower limit Q_{ll} on Q ; in this case x is equal to some constant $-C$, i.e.,

$$(Q_{\text{ll}} - N - 2)/\sqrt{2(N + 2)} = -C. \quad (3)$$

For large N , $\sum_{i=1}^N d_i^2 \approx \delta^2 N$ and assuming that $\sigma^2 \ll \delta^2$ we find for the upper limit σ_{ul} on σ

$$\sigma_{\text{ul}} \propto \delta N^{-1/4}. \quad (4)$$

In Figure 1, I test this analytic estimate with direct mock-data simulations and inferences. This figure demonstrates that the large- N asymptotic behavior occurs above about 100 data points, with a steeper dependence on N between 10 and 100 data points. The latter is the relevant regime for the data in this paper.

Thus, in the limit of many data points, it is difficult to significantly improve upon the upper limit on the intrinsic scatter by observing more stars, especially given the limited number of stars suitable for high-resolution spectroscopy in all but the nearest clusters. As Figure 1 illustrates, if one were to use the simplistic “0.1 dex” standard abundance uncertainty, about 100,000 stars would be required to limit the intrinsic dispersion to below 0.01 dex. It is therefore of the utmost importance to characterize, understand, and use one’s abundance precision.

The analytic estimate in this section and the simulations in Figure 1 also show that given a fixed amount of observing time T , it is more efficient to observe a small number of stars for longer times (uncertainties and the intrinsic-scatte limit decrease as $T^{-1/2}$) than to observe a large number of stars for short times (the intrinsic-scatte limit decreases as $T^{-1/4}$ if $N \propto T$), at least in the regime where the abundance uncertainties are limited by photon noise. Thus, higher signal-to-noise ratio observations of a smaller sample are more important.

1.2. Overview

Motivated by the discussion in the previous section that the abundance precision is of the highest importance in studying abundance scatter, and by the fact that data uncertainties are simplest in the space of the spectra themselves rather than in that of the measured abundances, I propose a novel method here for limiting the abundance scatter in clusters and for evaluating similarity and dissimilarity of abundances in groups of stars more generally. This method evaluates the effect of abundance scatter through forward modeling on the observed stellar spectra where it can be directly compared to the spectral uncertainties. By empirically removing temperature trends in both the observed and simulated spectra, this method is robust to modeling errors related to standard assumptions in stellar spectroscopy and to the main effects of stellar evolution on the surface abundances.

This paper is organized as follows. In § 2 I propose that a simple empirical model for an open cluster without intrinsic abundance scatter is that all stellar prop-

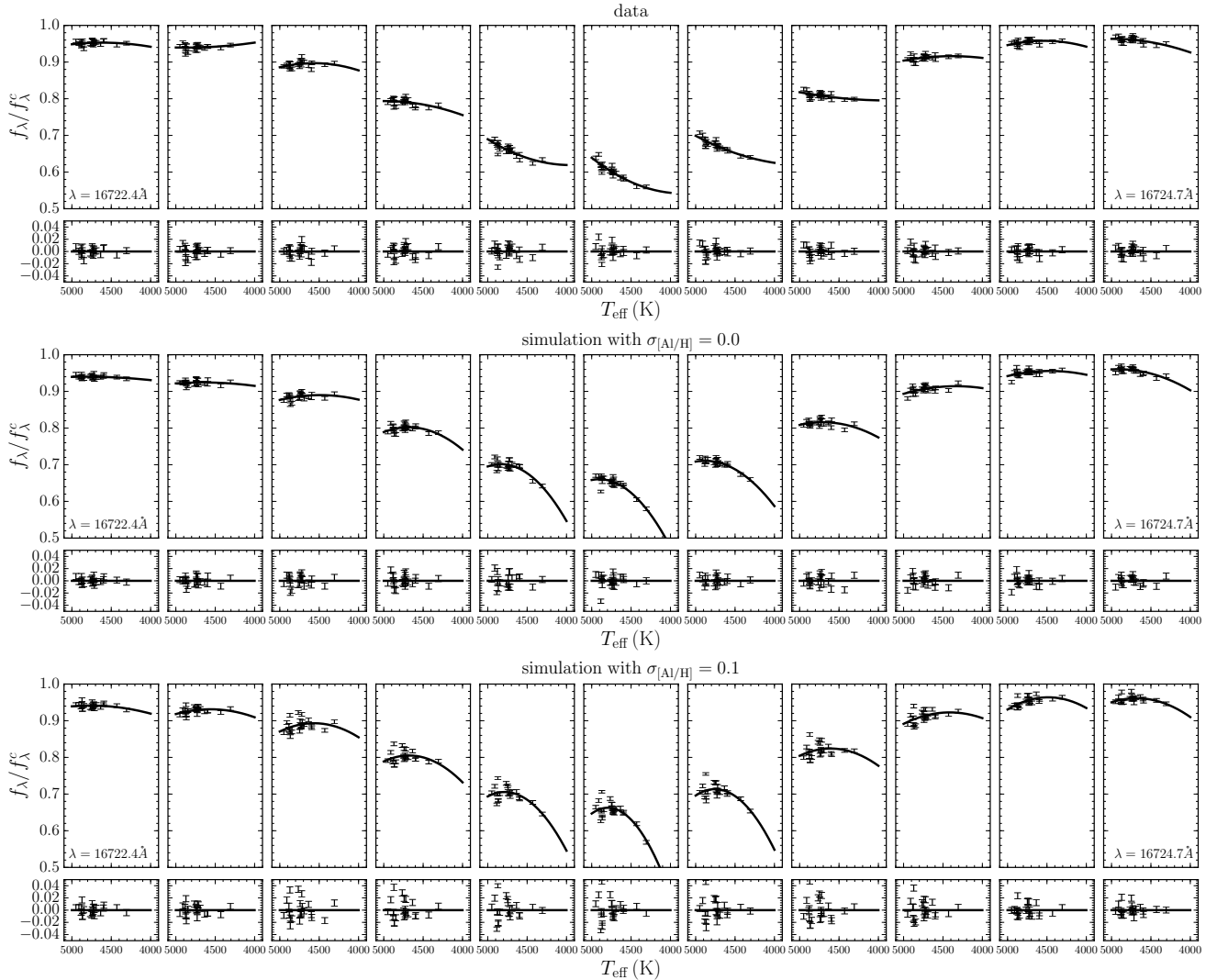


FIG. 2.— The Al spectral line at 16723.5 Å for giants in M67 (top). Each column displays the dependence of a single pixel of the continuum-normalized spectrum on T_{eff} and a quadratic fit to this dependence. The bottom panels show the residuals from the fit; these are largely consistent with the reported uncertainties. The bottom two sub-figures show the same for two simulations of the data: The middle figure assumes no intrinsic scatter in the Al abundance and the bottom figure uses a scatter of 0.1 dex. For the latter simulation, the residuals are clearly larger than the uncertainties, demonstrating that the scatter around the quadratic fit is strongly constraining for the intrinsic abundance scatter.

erties are a one-dimensional function of (fundamentally) initial mass and I discuss how we can easily test this model. § 3 introduces the APOGEE data for the four open clusters that the method in this paper is applied to. In § 4, I explicitly test the one-dimensional hypothesis for the APOGEE clusters. I demonstrate that all clusters are consistent with this hypothesis and that this is strongly constraining for the intrinsic scatter in 15 elements that have absorption features in the APOGEE wavelength range. To make the intrinsic-scatter limits precise, § 5 describes a method using Approximate Bayesian Computation (ABC) that uses detailed simulations of the observed spectra to put robust limits on the intrinsic abundance scatter. I discuss the results, their implications, and future prospects in § 6.

Appendix A displays the high signal-to-noise “stacked” red-giant spectra for M67, NGC 6819, and NGC 2420 that I obtain using the method in § 2. The remaining three appendices discuss relevant technical details

of the observed and synthetic APOGEE spectra. Appendix B discusses how I construct an empirical error model for the APOGEE continuum-normalized spectra using repeat observations of stars. Appendix C provides details of the procedure and code to generate synthetic APOGEE spectra tailored to each star for variations of all 15 considered elements. Appendix D presents an investigation of the sensitivity of APOGEE spectra to abundance changes of different elements; these sensitivities are a crucial ingredient in constraining the abundance scatter using forward simulations.

2. AN EMPIRICAL MODEL FOR THE SPECTRA OF OPEN-CLUSTER MEMBERS

The model for open clusters that we are interested in constraining is that they consist of a set of stars born from a well-mixed gas cloud in a negligible amount of time ($\lesssim 10$ Myr). Assuming no scatter in the birth abundances, the most important factor distinguishing differ-

ent stars is their different initial mass, which spans the range $\approx 0.1 M_{\odot}$ to $\approx 100 M_{\odot}$. Each star’s initial mass together with the common initial abundances determines its subsequent evolution. At the present day, we observe stars in clusters to span a wide range of luminosities, temperatures, surface gravities, etc. due to the range in initial masses. Every photometric and spectroscopic property of cluster stars should then follow a one-dimensional relation as a function of stellar mass. In particular, the spectra of cluster stars near absorption features of different elements should follow a one-dimensional sequence. Without any reference to particular models of stellar photospheres, this is a testable prediction.

An important advantage of this approach to testing the chemical homogeneity of open clusters, is that many of the stellar evolution effects on the surface abundances that normally confound studies of homogeneity by (correctly) showing abundance scatter in the *current* abundances (e.g., Önehag et al. 2014), are themselves primarily functions of the stellar mass (e.g., gravitational settling or mixing of C, N, and O during dredge-up episodes). Similarly, hydrodynamical effects often parametrized in simplified treatments using micro- and macroturbulence are mostly functions of the current evolutionary state (temperature, gravity) and therefore also functions of stellar mass. Theoretically predicting these functions is difficult, but it is clear that the combination remains one-dimensional and fitting a flexible one-dimensional model allows us to ignore this lack of knowledge.

Besides these deterministic effects, random effects in the initial condition of each star or in its subsequent evolution can break the one-dimensional model. For example, stars are born with a distribution of initial rotation speeds. When these survive to the present time, they will give rise to different line profiles. The effects of magnetic braking likely cause all stars in a cluster to have the same current rotation for the old clusters that we are interested in here (> 1 Gyr; Weber & Davis 1967; Skumanich 1972; Kawaler 1988), but a random distribution of inclinations will still give rise to different line profiles. For the giants that I consider in this paper, the line broadening due to rotation can, however, be neglected. Differences in initial rotation might additionally induce variations in the internal mixing that could manifest themselves at the surface today. Interactions between binary stars may also lead to abundance anomalies that would be uncorrelated with mass, or the infall of rocky planets could lead to scatter in the abundances of refractory elements (Meléndez et al. 2009). While this might confound studies of the initial chemical homogeneity of clusters, limits on the abundance scatter obviously constrain the importance of these processes.

Beyond effects intrinsic to the cluster stars, instrumental effects may give rise to scatter at fixed initial stellar mass, even when all stars are observed with the same instrument. Foremost among these are variations in the line-spread function (LSF), which lead to different broadening profiles similar to the case of rotation discussed above. For the APOGEE spectra that I employ in this paper, LSF variations exist, but are small enough that they are only confused with abundance scatter $\lesssim 0.01$ dex. In the forward modeling approach below,

I take the LSF variations among cluster stars fully into account.

The basic model that I will use in this paper is therefore that the spectra of stars in open clusters are a one-dimensional sequence. Because (initial) stellar mass is difficult to observe, I will employ the effective temperature T_{eff} as a proxy for the mass and use one-dimensional models as a function of temperature. For the red giants that we will consider later, T_{eff} is a good proxy for the mass¹ and we have photometric T_{eff} available that are independent of the considered spectra. Each pixel value f_{λ}^i for different stars $i = 1 \dots N$ in a cluster and wavelengths λ can then be modeled as a function $g_{\lambda}(T_{\text{eff}}|\theta_{\lambda})$ characterized by parameters θ_{λ} plus the measurement noise

$$f_{\lambda}^i = g_{\lambda}(T_{\text{eff},i}|\theta_{\lambda}) + \text{noise}. \quad (5)$$

I model g_{λ} as a second-order polynomial in T_{eff} and we can then fit for the parameters θ_{λ} at each wavelength using the observed f_{λ}^i and their catalog uncertainties using maximum likelihood; I also include an intrinsic scatter in the fit, but this is always small. This approach is similar to that taken by Ness et al. (2015) for deriving an empirical model of stellar spectra using a calibration sample that can then be applied to determine stellar parameters (T_{eff} in this case). The approach taken here is different in that I fit the empirical model only as a way of determining whether the spectra of stars in a cluster are the same apart from trends with T_{eff} .

Once we have determined the best-fitting $g_{\lambda}(T_{\text{eff},i}|\theta_{\lambda})$ for each pixel λ , we can compute the residuals which are given by

$$r_{\lambda}^i = f_{\lambda}^i - g_{\lambda}(T_{\text{eff},i}|\theta_{\lambda}). \quad (6)$$

If the one-dimensional model provides a good fit, then the distribution of residuals should be consistent with the uncertainty distribution for each pixel.

This procedure is illustrated in Figure 2. The ‘data’ row of this figure displays APOGEE spectra for stars in M67 (described in more detail below) in the region of an Al feature. Each column sub-panel shows the dependence of the observed flux on T_{eff} and the polynomial fit to this dependence. The bottom panels display the residuals from the fit and it is clear by eye that the residuals are largely consistent with the reported uncertainties.

3. DATA

The spectroscopic data for open-cluster members that I analyze here comes from the SDSS-III/APOGEE (Majewski et al. 2015), a high-resolution ($R \approx 22,500$) spectroscopic survey that observes in the H -band (1.51 to 1.70 μm) using a 300-fiber spectrograph (Wilson et al. 2010, J. Wilson et al. 2015, in preparation) on the 2.5-meter Sloan Foundation telescope (Gunn et al. 2006). I use data from the public Data Release 12 (DR12; Alam et al. 2015; Holtzman et al. 2015) for four open clusters that have a large number of members: M67 ($[\text{Fe}/\text{H}] \approx 0$), NGC 6819 ($[\text{Fe}/\text{H}] \approx 0$), NGC 2158 ($[\text{Fe}/\text{H}] \approx -0.15$), and NGC 2420 ($[\text{Fe}/\text{H}] \approx -0.2$). Members for these

¹ As we will see, this does not hold exactly because of the presence of both red-giant and red-clump stars at temperatures ≈ 4750 K. Red-clump stars have slightly different surface gravities at the same T_{eff} and may also have different C and N abundances due to the effect of convective mixing on the upper giant branch.

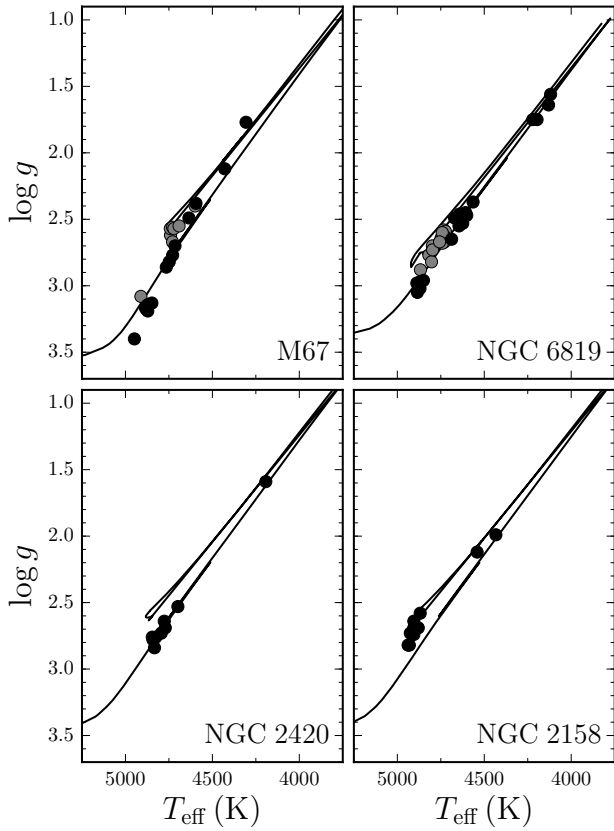


FIG. 3.— $\log g$ vs. T_{eff} for the four open clusters studied in this paper. Likely red-clump stars have been colored gray for M67 and NGC 6819. These are excluded for the analysis of C and N for M67 and are altogether excluded for the analysis of NGC 6819. PARSEC isochrones (Bressan et al. 2012) for ages of 2.5, 1.6, 2, and 2 Gyr at the cluster’s metallicity are shown as well.

clusters are obtained from the catalog in Mészáros et al. (2013) and I use the photometric T_{eff} , surface gravities $\log g$, and overall metallicities $[\text{Fe}/\text{H}]$ used in that paper. Full details on the APOGEE target selection for these clusters can be found in Zasowski et al. (2013). I only select the stars with $4000 \text{ K} \leq T_{\text{eff}} \leq 5000 \text{ K}$, because this range contains most of the stars and spectral modeling is more uncertain at $T_{\text{eff}} < 4000 \text{ K}$. After this cut, the sample consists of 24 stars, 8 of which are likely red-clump stars, for M67; 30 stars, 13 of which are likely red-clump stars, for NGC 6819; 10 stars in NGC 2158; and 9 stars in NGC 2420. The $\log g$ vs. T_{eff} for the giants in these clusters are displayed in Figure 3.

The spectra used here are the *apStar* spectra that combine data from all APOGEE observations of a given star; I use the version using a “global” weighting of the individual spectra going into the combination. These spectra are sampled on a logarithmic wavelength grid in the restframe of the star (Nidever et al. 2015). In Appendix B, I also use the spectra from the individual hour-long APOGEE observations that are combined to form the *apStar* spectra; these are also available from the SDSS data base on the same wavelength grid. Pixels identified as bad in the APOGEE.PIXMASK bitmask for the reasons BADPIX, CRPIX, SATPIX, UNFIXABLE, BADDARK, BADFLAT, BADERR, NOSKY, or SIG_SKYLINE (Holtzman et al. 2015) are given very large uncertainties to remove

them from further consideration. Uncertainties smaller than 0.5 % are set to 0.5 %, because of systematic errors at the 0.5 % level for APOGEE spectra (Nidever et al. 2015).

I fit for the continuum of each spectrum using the method of Ness et al. (2015). This method identifies a set of continuum pixels by fitting a quadratic model in $(T_{\text{eff}}, \log g, [\text{Fe}/\text{H}], [\alpha/\text{Fe}])$ to each pixel for a calibration sample with known $(T_{\text{eff}}, \log g, [\text{Fe}/\text{H}], [\alpha/\text{Fe}])$ and selecting those pixels whose values display only a small dependence on $(T_{\text{eff}}, \log g, [\text{Fe}/\text{H}], [\alpha/\text{Fe}])$. I use the same calibration sample as used in Ness et al. (2015) and select pixels with linear dependencies less than $(10^{-5} \text{ K}, 0.006, 0.012, 0.03)$ in $(T_{\text{eff}}, \log g, [\text{Fe}/\text{H}], [\alpha/\text{Fe}])$ (similar to Ness et al. 2015) and additionally limit the pixels to those with intrinsic scatter less than 0.015 to remove pixels with large variations that cannot be attributed to the basic stellar parameters. Using the wavelengths of these continuum pixels, the continuum for each star is determined by fitting a fourth-order polynomial over the wavelength range of each of the three APOGEE detectors to just these wavelengths. As demonstrated in Appendix B using repeat observations, this procedure is highly stable and produces consistent continuum-normalized spectra for different observations of the same star. After continuum normalization, uncertainties smaller than 0.005 are set to 0.005 for the same reason as above. I further remove pixels with errors larger than 0.02 (signal-to-noise ratio < 50) from further consideration, because the errors for these low signal-to-noise ratio pixels might not be well-characterized by the reported uncertainty (this includes all of the pixels flagged as bad mentioned earlier). This only removes a few percent of the pixels.

Ideally, the errors in the spectra should be well-characterized by the reported uncertainties in the APOGEE database, which assume uncorrelated errors between different pixels. I test the reported uncertainties in Appendix B using 4,143 repeat observations of 1,381 stars bright enough that each individual hour-long exposure has high signal-to-noise ratio. These tests demonstrate that the reported uncertainties are typically underestimated by 10 to 20 %, but ranging up to 100 % for significant portions of the wavelength range, especially near the ubiquitous telluric absorption features. Furthermore, these tests show that errors display significant correlations out to dozens of pixels ($\gtrsim 10 \text{ \AA}$). This is a range that is almost ten times as wide as the reported LSF. This large range over which correlations are significant is most likely due to correlated errors induced by the continuum normalization. In what follows I use the residuals from repeat observations directly as an empirical sampling of the uncertainty in the observed spectra (see further discussion in Appendix B).

Appendix C discusses the details of how I generate synthetic APOGEE spectra for each cluster star individually using its $(T_{\text{eff}}, \log g)$, the median cluster metallicity, and variations in the abundances of individual elements. Using these synthetic spectra, we can estimate the precision with which we can measure the abundances of individual elements by computing the $\Delta\chi^2([X/\text{H}])$ from a baseline model where all abundance ratios are solar. I compute this $\chi^2([X/\text{H}])$ weighting the contribution of each pixel

TABLE 1
EXPECTED ABUNDANCE UNCERTAINTIES

Element	M67	NGC 6819	NGC 2420
C	0.04 (0.03–0.07)	0.05 (0.02–0.07)	0.06 (0.02–0.07)
N	0.07 (0.06–0.09)	0.06 (0.04–0.08)	0.08 (0.05–0.08)
O	0.16 (0.04–0.20)	0.13 (0.04–0.20)	0.16 (0.03–0.20)
Na	0.13 (0.08–0.17)	0.09 (0.06–0.12)	0.16 (0.09–0.20)
Mg	0.04 (0.03–0.05)	0.03 (0.03–0.04)	0.03 (0.03–0.04)
Al	0.09 (0.08–0.10)	0.04 (0.04–0.04)	0.04 (0.04–0.05)
Si	0.06 (0.06–0.06)	0.04 (0.04–0.05)	0.04 (0.04–0.05)
S	0.12 (0.11–0.20)	0.07 (0.07–0.09)	0.08 (0.08–0.11)
K	0.06 (0.06–0.07)	0.04 (0.03–0.04)	0.04 (0.04–0.04)
Ca	0.05 (0.04–0.05)	0.04 (0.04–0.04)	0.04 (0.04–0.04)
Ti	0.07 (0.05–0.10)	0.06 (0.04–0.09)	0.10 (0.04–0.12)
V	0.08 (0.03–0.14)	0.08 (0.03–0.13)	0.15 (0.04–0.20)
Mn	0.06 (0.05–0.07)	0.03 (0.03–0.04)	0.06 (0.04–0.06)
Fe	0.06 (0.05–0.06)	0.04 (0.04–0.04)	0.04 (0.04–0.04)
Ni	0.07 (0.07–0.07)	0.06 (0.05–0.06)	0.06 (0.06–0.06)

NOTE. — Expected abundance uncertainties in the abundance of X computed from $\Delta\chi^2(X)$ (weighted using the pixel weights of Appendix D) of a baseline model with solar abundance ratios for each cluster star. The median precision for each element and each cluster is shown, as well as the full range of all the cluster members in parenthesis. These precisions assume perfect spectral models, perfect knowledge of all other stellar parameters and abundances, and that the APOGEE noise model is correct, but by using the pixel weights they only use parts of the spectrum that are sensitive to each element. Therefore, these represent a realistic estimate of the expected precision that can be hoped to be achieved.

with the pixel-weights that give prominence to clean absorption features of each element (see Appendix D). Assuming perfect knowledge of all other parameters (T_{eff} , $\log g$, $[\text{Fe}/\text{H}]$, but also micro- and macroturbulence, etc.) and that our modeling is perfect, this effectively sets a realistic lower limit on the precision. I compute $\chi^2(X/\text{H})$ using the reported uncertainties (i.e., not taking into the account the underestimation of the uncertainties), which also makes the estimated abundance uncertainties a lower limit. These estimated abundance uncertainties are shown in Table 1. From Figure 1, we expect the 95 % upper limit on the abundance scatter in each individual cluster to be roughly the precision of an individual abundance measurement (slightly smaller for M67 and NGC 6819, slightly larger for NGC 2420). The precision for some elements (like C, N, and O) sensitively depends on temperatures, leading to a wide range of expected precision. If we combine all clusters, the ~ 50 stars should give a 95 % upper limit that is about 60 % of the abundance precision. It is therefore clear that we should be able to extract limits on the intrinsic abundance scatter for most of these elements at the level of a few times 0.01 dex.

4. ARE OPEN CLUSTERS ONE-DIMENSIONAL SEQUENCES?

To check whether or not the four open clusters described in § 3 are consistent with forming a one-dimensional temperature (as a proxy for mass) sequence, I fit the quadratic model to the T_{eff} dependence of each pixel using members in each cluster as discussed in § 2. M67 and NGC 6819 both have a significant number of both red-clump and first-ascent red-giant stars at similar temperatures (see Figure 3). These lead to two potential issues with the method used in this paper. Firstly, deep mixing along the upper giant branch (e.g., Gilroy & Brown 1991) can change the surface C and N abun-

dances. While this should be a smooth change as a function of temperature, when stars move to the red-clump after the helium flash, as a function of temperature alone this leads to stars in the cluster having a bimodal C and N distribution that cannot be captured with the model from § 2. Secondly, red-clump stars have slightly lower $\log g$ than first-ascent red-giant stars at the same T_{eff} . This again leads to variations in the spectra at a fixed T_{eff} that are not included in our model. To avoid these issues, I remove all red-clump stars in M67 when looking at C and N, but not when considering the other elements. The number of red-clump giants is large enough in NGC 6819 that their $\log g$ differences lead to substantial scatter and I therefore remove all clump giants altogether in NGC 6819. If we were to fit the spectra as a function of mass rather than T_{eff} , these issues would be avoided, but we currently do not have precise enough masses to do this. In NGC 6819, I also remove the Li-rich giant 2M19411367+4003382, which may not be a cluster member or has anomalously low mass if it is (Carlberg et al. 2015). The final sample for NGC 6819 therefore consists of 16 stars.

I further find through visual inspection that the spectra of stars in NGC 2158 have significant issues with continuum normalization due to a large fraction of bad pixels. The regions with bad continuum normalization are identified by eye and removed from further consideration. The remaining data is for so few stars and so few pixels that no interesting constraints on the abundance scatter can be placed. I discuss the results for NGC 2158 in this section, but do not consider it further.

Thus, I compute the residuals from the quadratic fit for all pixels (see Figure 2 for an illustration of the quadratic fit and its residuals for pixels near an Al line) and normalize them using the reported pixel-level uncertainties. The cumulative distribution of all normalized residuals for all four clusters are displayed in the top, left panel of Figure 4. They are compared with the distribution of normalized residuals from repeat observations, which give the distribution expected from random errors in the spectra alone (see Appendix B). These noise residuals have a very similar distribution to those from the quadratic fit; the noise line cannot be seen because it lies underneath those from the four clusters.

The other panels in Figure 4 show the same residuals, but weighted using the pixel-level weights for different elements described in Appendix D. These weights for a given element essentially correspond to the derivatives of model spectra with respect to the abundance of that element. Thus, these panels display the residuals in regions dominated by the effects of a given element, giving higher weight to those pixels which are most strongly affected by changes in that element. We see that the distribution of fit residuals is consistent with that of the noise residuals for practically all elements and all clusters. For comparison, I have also performed the same kind of fit for 62 members of M13, a globular cluster that displays significant anti-correlations in its light-element abundances (see Mészáros et al. 2015 for a study of this using the APOGEE data). The distribution of residuals for M13 is shown for the light elements (atomic number < 14). It is clear that a significant dispersion in C, N, O, Mg, and Al is present for M13 (that for Na cannot be detected, because the Na line used here is too weak at the

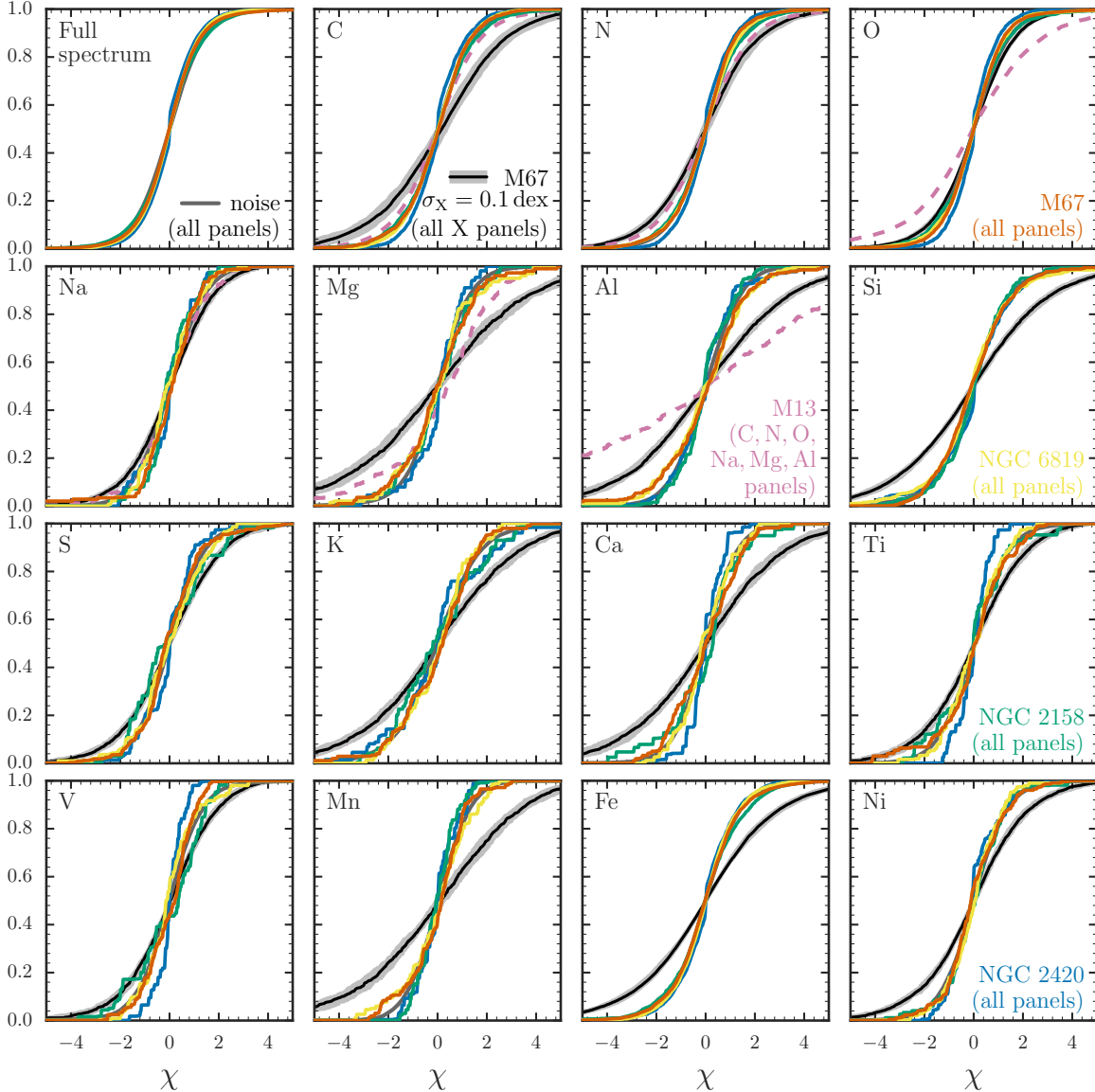


FIG. 4.— Cumulative distribution of the normalized residuals from the quadratic T_{eff} fit to each pixel of the continuum-normalized spectra for members of the open clusters M67, NGC 6819, NGC 2158, and NGC 2420. The top, left panel shows the cumulative distribution of all pixels in the spectrum. The other panels display the same residuals, but weighted using the pixel weights that give prominence to the pixels most affected by a given element (see Appendix D). The color-coding of the different clusters is indicated by the text labels. The dark gray line shows the distribution of normalized residuals due to errors in the spectra derived from repeat observations (see Appendix B); this line cannot be clearly seen in most panels because it lies beneath the curves for the four open clusters. The dashed line shows the residuals computed using a similar quadratic fit for M13, a globular cluster with known scatter and anti-correlations in the abundances of light elements (these are only shown for C, N, O, Na, Mg, and Al). The black line and light gray band give the median and interquartile range of simulated data for M67 with an abundance spread of $\sigma_{[\text{X}/\text{H}]} = 0.1$ dex. The distribution of residuals around the one-dimensional T_{eff} fit for all clusters is consistent with that expected from the random errors in the spectra for all elements. An abundance scatter of 0.1 dex in any of the 15 elements considered here would give rise to much larger residuals.

metallicity of M13).

Thus, we see that the spectra of members of all four open clusters are consistent to within their uncertainties with forming a one-dimensional function of T_{eff} . I do not attempt to quantify this consistency further here, but instead directly infer constraints on the abundance scatter using a similar method in § 5. To get a sense of how strong a constraint on the abundance scatter of different elements this consistency implies, I have computed 100 sets of mock spectra for all M67 stars assuming an

intrinsic scatter of $\sigma_{[\text{X}/\text{H}]} = 0.1$ dex using the procedure described in Appendix C and have fit each set with the same quadratic T_{eff} model as the real data. An example simulation is displayed in the bottom panel of Figure 2. The median and interquartile range of these 100 simulations for each element is shown in Figure 4. For all elements a scatter of 0.1 dex would give a distribution of the normalized residuals that is much wider than the observed distribution for M67 and that is much wider than can be explained by the errors in the spectra.

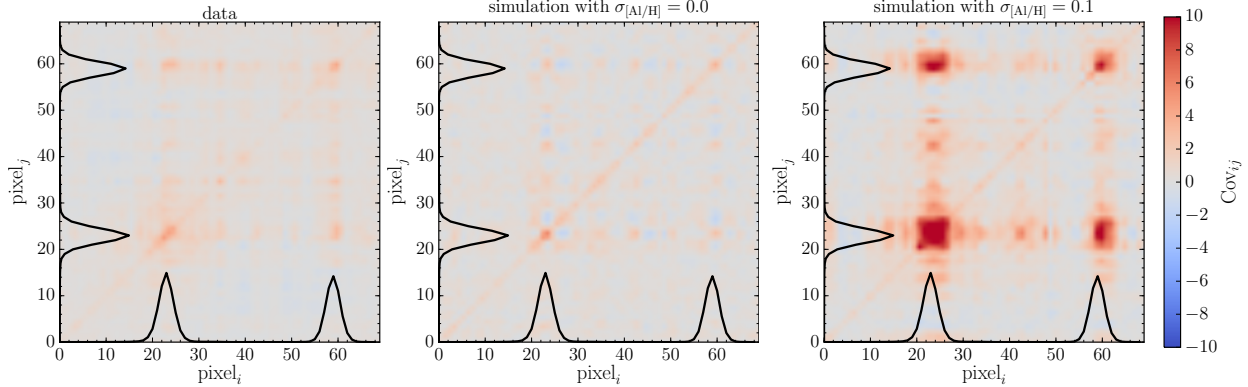


FIG. 5.— Covariance matrix of the normalized residuals of the data for members of M67 (left panel) and for the simulations assuming $\sigma_{[\text{Al}/\text{H}]} = 0$ (middle panel) and $\sigma_{[\text{Al}/\text{H}]} = 0.1$ dex from Figure 2. Only the 69 pixels with non-zero Al weights are included. The Al weights are displayed as the black lines on both the x and y axis; these peak at the two Al lines used here. Intrinsic abundance scatter in Al leads to a large scatter in the residuals near the Al line and to large correlations between the residuals at different absorption wavelengths that can be used to constrain the intrinsic abundance scatter.

As the spectra of all cluster members are consistent with being the same except for their temperatures, we can use the quadratic fit to construct a high signal-to-noise ratio spectrum for the cluster at a given temperature. This combined *cluster spectrum* at $T_{\text{eff}} = 4750$ K for the red giants in M67, NGC 6819, and NGC 2420 is displayed and discussed in Appendix A.

5. INFERENCE OF THE ABUNDANCE SCATTER

To determine constraints on the abundance scatter of different elements for each cluster, I use Approximate Bayesian Computation (ABC) to construct an approximation of the posterior probability distribution function (PDF) of the scatter $\sigma_{[\text{X}/\text{H}]}$ in each element X. ABC is an inference technique that approximates the PDF without explicitly evaluating the likelihood, but instead making use of forward simulations of the data. To explicitly evaluate the likelihood of $\sigma_{[\text{X}/\text{H}]}$ would require an actual model for the noise in the spectra—which is difficult to establish (see Appendix B)—and it would be computationally expensive, because we would need to marginalize over the individual abundances of each cluster member, while properly taking into account the varying LSF. However, it is straightforward to generate simulated data for any $\sigma_{[\text{X}/\text{H}]}$ that take into account LSF variations, the noise and its correlations in the spectra, and that are robust against systematics in the abundances due to, e.g., deep mixing or deviations from local thermodynamic equilibrium.

For any $\sigma_{[\text{X}/\text{H}]}$, I draw a set of N abundances $[\text{X}/\text{Fe}]$ for the N cluster members, generate synthetic spectra using the procedure described in Appendix C, and then fit the T_{eff} dependence of each pixel using the quadratic model described in § 2 in the same way as for the data. An example of this is displayed for one of the Al lines in Figure 2. The top panel of that figure shows the data, while the middle and bottom panels show simulated data with $\sigma_{[\text{X}/\text{H}]} = 0.0$ dex and $\sigma_{[\text{X}/\text{H}]} = 0.1$ dex, respectively. When running ABC, we retain those $\sigma_{[\text{X}/\text{H}]}$ that lead to similar residuals from the quadratic fit as found in the data. By only considering a match between the data and the simulated data in terms of their residuals, we focus the comparison on the abundance scatter, rather

than on whether the simulations produce the exact same continuum levels, the same line strengths (which may be affected by such effects as deviations from local thermodynamic equilibrium or hyperfine structure), the correct behavior of weak and strong lines of a given element, and whether evolutionary changes in the surface abundances are included.

ABC produces an approximation to the PDF by (a) simulating $\sigma_{[\text{X}/\text{H}]}$ from its prior (which I take to be uniform between 0 and 0.1 dex), and (b) only storing those $\sigma_{[\text{X}/\text{H}]}$ that lead to simulated data that are “the same” as the real data (Tavaré et al. 1997; Pritchard et al. 1999). By considering the meaning of the PDF (“the probability distribution of $\sigma_{[\text{X}/\text{H}]}$ given the data”), it is clear that this procedure works, because it generates a Monte Carlo sampling of $\sigma_{[\text{X}/\text{H}]}$ that are constrained to be the same as the data and are therefore a sampling of the PDF. See, for example, Marin et al. (2012) for a recent review of ABC.

ABC requires one to specify what it means for simulated data D' to be same as the actual data D . This is done by defining a metric $\rho(D', D)$ that expresses how close the simulated data are to the real data. The PDF for $\sigma_{[\text{X}/\text{H}]}$ is constructed using the $\sigma_{[\text{X}/\text{H}]}$ that generate D' that satisfy $\rho(D', D) \leq \epsilon$ and ABC produces an exact sampling of the PDF in the limit $\epsilon \rightarrow 0$. Of course, it is difficult to generate simulated data that are exactly like the actual data, especially in the presence of random noise. If the data and model have a lower-dimensional sufficient statistic $\mu(D)$ that encapsulates all of the information about $\sigma_{[\text{X}/\text{H}]}$ that is contained in the data, this situation is significantly ameliorated. While a rigorous sufficient statistic does not exist for the problem considered in this paper, as I argue below there are summary statistics that can be used to significantly reduce the dimensionality of the data and make this problem tractable for ABC.

In principle, we need to constrain all 15 $\sigma_{[\text{X}/\text{H}]}$ simultaneously, because all 15 elements affect the spectra and disentangling their effects is difficult, especially for C, N, and O. Because I only derive upper limits on $\sigma_{[\text{X}/\text{H}]}$, however, I can consider each element separately. That is, the lack of scatter in the spectra near, e.g., CN fea-

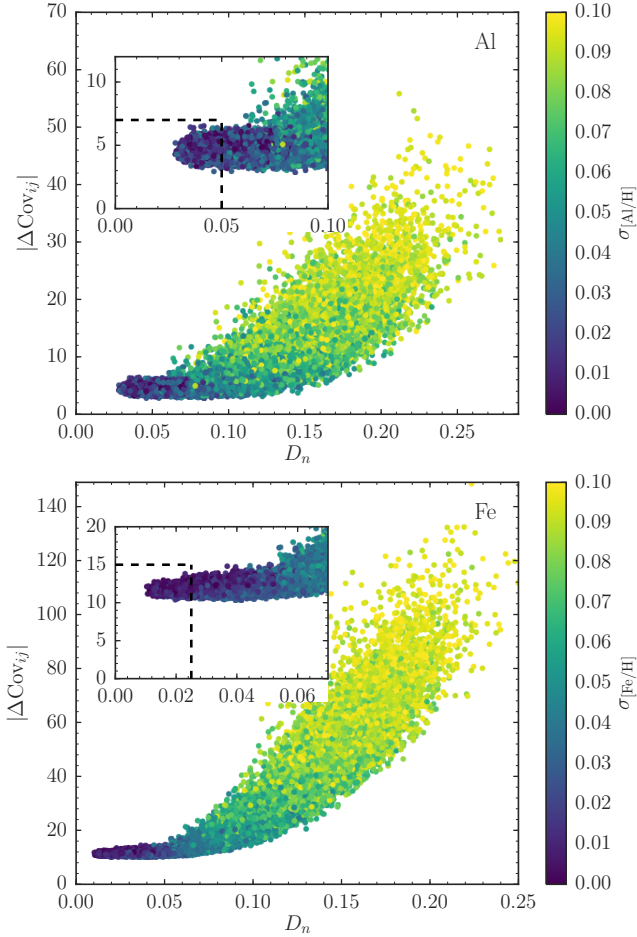


FIG. 6.— Two summary statistics employed in the ABC simulations in § 5 to evaluate the similarity between the data and the simulated data. The top panel shows simulations with intrinsic scatter in Al and the bottom panel has simulations with scatter in Fe, both for stars in M67. The x axis is the Kolmogorov-Smirnov distance D_n between the cumulative distribution of the normalized residuals of the data and the simulated data (see Figure 4). The y axis has the difference $|\Delta\text{Cov}_{ij}|$ between the covariance matrix of the residuals of the data and the simulated data. Both summary statistics use residuals that are weighted using the weights for Al in the top panel and Fe in the bottom panel. The simulations are color-coded by their value of $\sigma_{[X/H]}$. Especially $|\Delta\text{Cov}_{ij}|$ is an excellent summary statistic and is strongly correlated with $\sigma_{[X/H]}$, leading to strong constraints on $\sigma_{[X/H]}$. Using the statistic D_n adds information on the shape of the distribution of residuals as well. The inset zooms in on those simulations that are closest to the data and the dashed lines display the cuts used to define the final $\sigma_{[X/H]}$ ABC sampling.

tures implies a limit on both $\sigma_{[C/H]}$ and $\sigma_{[N/H]}$ that can be established by varying $\sigma_{[C/H]}$ and $\sigma_{[N/H]}$ separately. Stronger, covariant limits on $\sigma_{[C/H]}$ and $\sigma_{[N/H]}$ could be determined by considering them simultaneously, but I do not attempt this here as it significantly increases the computational complexity. Similarly, we need not worry too much about whether the limit ϵ used to decide which simulated data are close to the actual data is a good limit, because setting it too high will only weaken the upper limits on $\sigma_{[X/H]}$.

I consider two summary statistics when running the ABC simulations. The first is the Kolmogorov-Smirnov distance D_n between the cumulative distribution of nor-

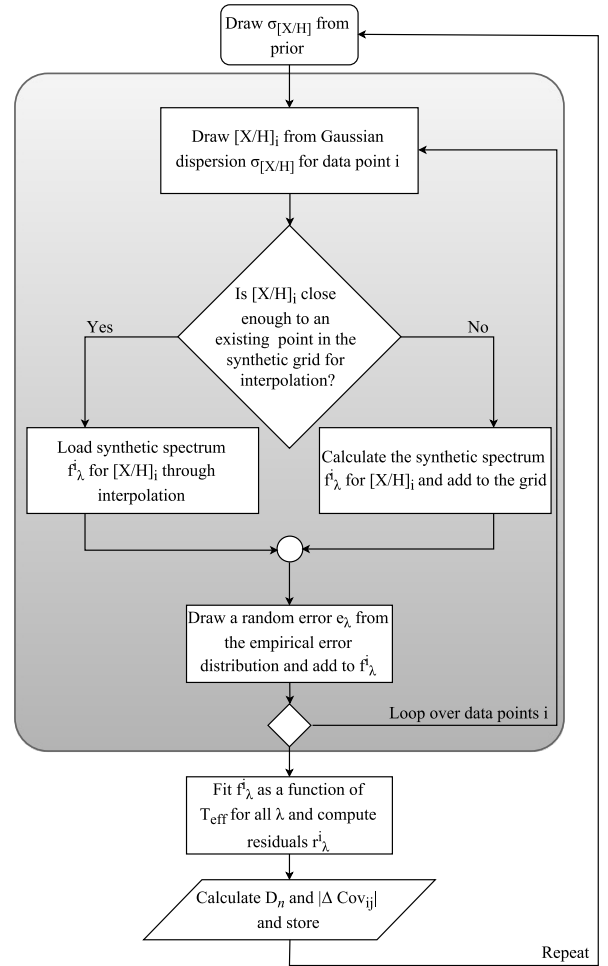


FIG. 7.— Overview of the steps involved in running a single ABC simulation. This procedure is repeated until a large number of simulations that pass the cuts in D_n and $|\Delta\text{Cov}_{ij}|$ are obtained.

malized residuals of the data and the simulated data, that is, the maximum difference between these distributions. For each element, these cumulative distributions are computed by weighting the residuals by the weights for that element (see Appendix D). For the data these cumulative distributions are shown in Figure 4. This figure also displays the median and interquartile range of the cumulative distributions of simulated data computed for $\sigma_{[X/H]} = 0.1$ dex.

The second summary statistic that I employ is based on the covariance matrix of the normalized residuals of different pixels. For the data and the simulated data, I compute the covariance matrix Cov_{ij} between pixels i and j . For each simulated data set, I calculate the difference

$$|\Delta\text{Cov}_{ij}| = \sqrt{\sum_{ij} (w_i w_j)^{1/2} (\text{Cov}_{ij}^{\text{data}} - \text{Cov}_{ij}^{\text{sim. data}})^2}, \quad (7)$$

where w_i and w_j are the weights for a given element. The covariance matrix Cov_{ij} for the data in M67 and for the two simulated data sets from Figure 2 are displayed in Figure 5. It is clear that $|\Delta\text{Cov}_{ij}|$ is a good sufficient statistic, especially for elements with many absorption features, because any abundance scatter in a given ele-

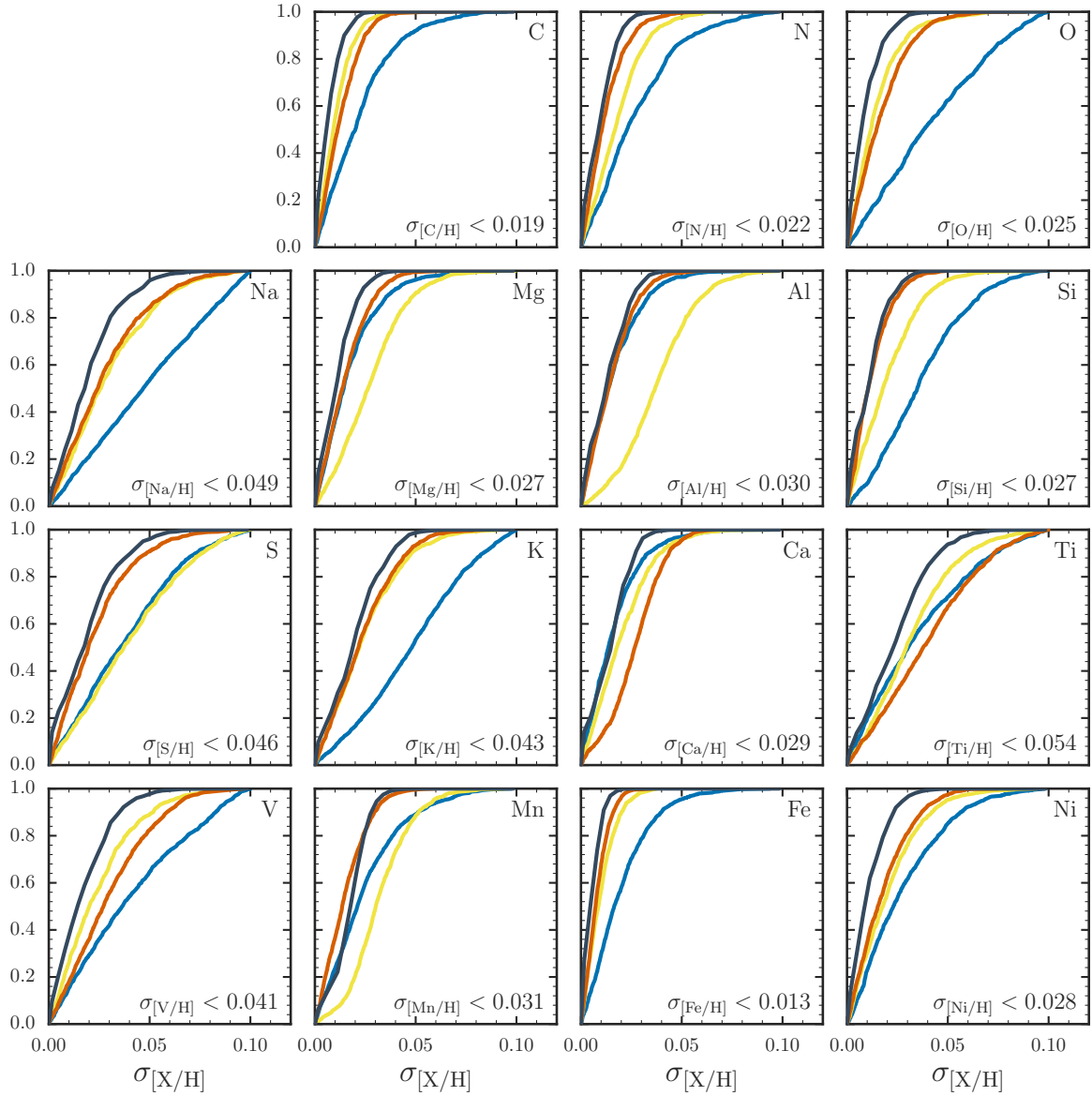


FIG. 8.— Cumulative posterior distribution functions for the intrinsic abundance scatter in 15 elements obtained from the ABC simulations. The color-coding of the three clusters is the same as in Figure 4: M67 is in red, NGC 6819 is in yellow, and NGC 2420 is in blue. The black curve gives the cumulative distribution function from the combination of all three clusters; the 95 % upper limit from this combined PDF is given in each panel. The 68 % and 95 % upper limits for all three clusters and the combined PDF are given in Table 2.

ment will give rise to correlated residuals at the positions of absorption features of that element. For example, in Figure 5, the simulated data with $\sigma_{[\text{Al}/\text{H}]} = 0.1$ dex has both large scatter at the positions of the Al lines, *and* large off-diagonal correlations between pixels in different lines. The fact that these are absent for the data puts a strong constraint on the Al scatter in M67.

As discussed in § 2, variations in the LSF for different stars can give rise to scatter in the residuals. While the mock-data simulations take any LSF variations for APOGEE into account, neither of the two summary statistics corrects for the effect of LSF variations. Doing so would require a metric function $\rho(D', D)$ that distinguishes between stars with different LSFs. Alternatively, a procedure to homogenize the LSF could be applied to both the data and the simulated data (in its crud-

est form, this would consist of convolving all data to the worst LSF). The effect of LSF variations can be seen in the zero-scatter simulation in the middle panel of Figure 5 as the regions of negative correlation surrounding the line centers and the positive correlation between the central pixels of the two Al lines shown. These features are absent in simulations using the same LSF for all stars.

The distribution of these two summary statistics in the ABC simulations for M67 are shown in Figure 6 for Al and Fe. It is clear that $|\Delta\text{Cov}_{ij}|$ is a good summary statistic, especially at large intrinsic scatter, as it strongly correlates with $\sigma_{[\text{X}/\text{H}]}$. The statistic D_n distinguishes between different $\sigma_{[\text{X}/\text{H}]}$ to a lesser extent, but is important for identifying those simulations that are most like the data, as D_n captures some of the information in the shape of the distribution of residuals that is

not captured by $|\Delta\text{Cov}_{ij}|$.

To construct the PDF for $\sigma_{[X/H]}$ for each element X and each cluster, I then run ABC simulations as described above. A flowchart of how these simulations are run is given in Figure 7. Before the start of each simulation, I compute a fine grid in $[X/H]$ from -0.20 dex to $+0.20$ dex with respect to the standard cluster abundances (median $[\text{Fe}/H]$ of all cluster members with solar abundance ratios) with a spacing of 0.01 dex; this grid is computed for each star individually. Subsequent simulations that require $[X/H]$ within the grid use linear interpolation to generate the spectra; spectra for $[X/H]$ outside of the grid are computed on-the-fly and added to the grid; interpolation is only ever performed for $[X/H]$ located between grid points within 0.01 dex from the nearest grid points. Each simulation then proceeds by drawing a $\sigma_{[X/H]}$ from the prior (uniformly between 0 and 0.1 dex), generating simulated spectra, performing the quadratic T_{eff} fit for each pixel, and computing the two summary statistics D_n and $|\Delta\text{Cov}_{ij}|$.

Good limits on D_n and $|\Delta\text{Cov}_{ij}|$ are determined by inspecting their distribution by eye and I run ABC simulations until the distributions appear to have converged (that is, small changes in the limits on D_n and $|\Delta\text{Cov}_{ij}|$ stop mattering) and until about $1,000$ $\sigma_{[X/H]}$ samples from the PDF have accrued. The limits on D_n and $|\Delta\text{Cov}_{ij}|$ for Al and Fe in M67 are displayed as dashed lines in Figure 6.

I have performed tests of the code verifying that no constraints on the abundance scatter are possible in the following limiting cases: (a) When only using three stars in a cluster, because then the quadratic fit is always perfect; and (b) when calculating the D_n and $|\Delta\text{Cov}_{ij}|$ summary statistics using the weights of a different element than the one whose intrinsic scatter is being constrained (choosing two elements with no overlapping weights, like Al and C or Ca and Mn), because then the statistics are not sensitive to abundance variations. All of such tests passed.

The cumulative distributions of the PDF for each element and each cluster are displayed in Figure 8. The 68 % and 95 % upper limits for each individual cluster are given in Table 2. The cumulative PDFs in Figure 8 demonstrate that we obtain strong limits on the abundance scatter, especially in M67 and NGC 6819, where we have the most cluster members. All elements are consistent with having no scatter; only for Ca in M67 and Al and Mn in NGC 6819 do the cumulative PDFs have a mild preference for a scatter of ≈ 0.03 dex, but with a tail toward zero scatter. Multiple elements for NGC 2420 have an almost flat PDF, especially O, Na, and K; this is simply due to the fact that these features are very weak in this more metal-poor cluster and that only a single low- T_{eff} star is included (for which we can get a precise O abundance).

From the results in Table 2, we see that for M67 and NGC 6819 we obtain strong constraints on the scatter in C, N, O, Mg, Al, Si, Mn, Fe, and Ni. We obtain weaker constraints for Na, S, K, Ca, Ti, and V and also obtain weaker results overall for NGC 2420. Given that I find no evidence for any abundance scatter in any of the clusters, it is reasonable to combine the PDFs into joint constraints on the abundance scatter (assuming all clus-

TABLE 2
LIMITS ON INTRINSIC ABUNDANCE SCATTER

	M67		NGC 6819		NGC 2420		Combined	
	68%	95%	68%	95%	68%	95%	68%	95%
C	0.016	0.030	0.013	0.025	0.027	0.058	0.009	0.019
N	0.015	0.031	0.023	0.043	0.034	0.069	0.013	0.022
O	0.022	0.041	0.017	0.039	0.055	0.088	0.010	0.025
Na	0.035	0.069	0.037	0.070	0.065	0.094	0.025	0.049
Mg	0.019	0.036	0.034	0.059	0.021	0.045	0.014	0.027
Al	0.019	0.035	0.045	0.069	0.020	0.041	0.018	0.030
Si	0.015	0.030	0.026	0.048	0.045	0.077	0.014	0.027
S	0.028	0.058	0.052	0.085	0.050	0.084	0.024	0.046
K	0.030	0.053	0.030	0.059	0.061	0.091	0.025	0.043
Ca	0.033	0.049	0.026	0.047	0.020	0.042	0.019	0.029
Ti	0.051	0.083	0.039	0.070	0.046	0.084	0.031	0.054
V	0.038	0.066	0.030	0.061	0.053	0.089	0.022	0.041
Mn	0.019	0.034	0.038	0.059	0.030	0.063	0.021	0.031
Fe	0.010	0.019	0.012	0.025	0.024	0.048	0.007	0.013
Ni	0.022	0.045	0.025	0.049	0.035	0.068	0.014	0.028

NOTE. — The 68 % and 95 % upper limits on the intrinsic abundance scatter in 15 elements. Those obtained from each individual cluster are given as well as those from combining all clusters.

ters have the same intrinsic scatter and placing a limit on this). The PDF obtained from combining the PDFs of all three clusters and the 95 % upper limits on $\sigma_{[X/H]}$ from this combined PDF are indicated in Figure 8; the combined constraints are also included in Table 2. We see that the combined constraints are strong. With the exception of Ti, all elements have a scatter constrained to be less than 0.05 dex at 95 % confidence.

The constraints on Fe and C are particularly strong: any intrinsic scatter has to be < 0.007 dex and < 0.009 dex in Fe and C, respectively, at 68 % confidence (< 0.013 dex and < 0.019 dex at 95 % confidence). We also obtain strong constraints on the intrinsic scatter in N and O, which has to be < 0.013 dex and < 0.010 dex, respectively, at 68 % confidence (< 0.022 dex and < 0.025 dex at 95 % confidence). That I find the strongest limits on C, N, O, and Fe is not surprising, because these elements have by far the most abundant absorption features in the near-infrared wavelength region used here, but the fact that I have been able to extract these constraints from the complicated molecular features for C, N, and O and in the light of deep mixing along the giant branch, demonstrates the power of the method developed here.

I also obtain strong limits on the scatter in Mg, Si, and Ni; these are all roughly $\lesssim 0.015$ dex and $\lesssim 0.03$ dex at 68 % and 95 % confidence, respectively. The limits on the scatter in Al, Ca, and Mn are less strong, but are nevertheless $\lesssim 0.02$ dex and $\lesssim 0.03$ dex at 68 % and 95 % confidence. The weaker features of Na, S, K, Ti, and V give weaker limits that are about 0.025 to 0.03 dex at 68 % and about 0.05 dex at 95 % confidence.

6. DISCUSSION AND CONCLUSIONS

6.1. Prospects for chemical tagging

The novel technique introduced here for constraining the abundance scatter in open clusters has several advantages over traditional techniques that determine each individual star's abundances and constrain the scatter in these abundances. Firstly, the new technique is robust to systematic uncertainties in the abundances stemming from the fact that obtaining consistent abundances over

wide ranges of stellar types is difficult. The systematics introduced by, e.g., deviations from the assumptions of local thermodynamic equilibrium, one-dimensional radiative transfer, and uncertainties in the line list will cause offsets in the abundances that are smooth functions of stellar mass (or here specifically, T_{eff}). By remaining agnostic about the overall T_{eff} trends of the spectra of the cluster members analyzed here, I avoid all of these issues directly. Secondly, many of the stellar-evolutionary effects on the surface abundances due to, e.g., deep mixing or gravitational settling, also change the abundances in a manner that is perhaps not well understood, but that is largely a deterministic function of the stellar mass. Therefore, I was able to constrain the *initial* abundance scatter rather than the present-day scatter and in particular constrain the scatter in C and N. Thirdly, the use of forward simulations and ABC makes it straightforward to include a large variety of real-world complications in the observed spectra such as non-Gaussian and variable LSFs, correlated noise in the spectra, and uncertainties coming from the applied continuum normalization.

It is easy to think of factors that should lead to a breakdown of the one-dimensional assumption that I propose here for clusters. The large spread in initial rotation velocities will give rise to differences in the spectra of young-cluster members that are largely orthogonal to those from differences in the initial mass. While the initial differences in rotation speeds will have largely disappeared due to magnetic braking for older open clusters (Kawaler 1988), the effect of the different viewing angles would still give rise to scatter in the spectra and for the technique used in this paper to work, the $v \sin i$ of each star probably needs to be inferred prior to the forward simulations. For the giants that I studied here, rotational velocities are small and I was therefore able to ignore this complication. Beyond the effects of the current velocity, initial velocity differences may still lead to spectral scatter today if they led to different mixing histories, changing the surface abundances of, e.g., C, N, and Li (Pinsonneault et al. 1990; Meynet & Maeder 2002). Effects of binarity and, in particular, of mass transfer between binary companions could also induce spectral scatter which would be difficult to correct.

The fact that I empirically determine that all open clusters are consistent with being one-dimensional sequences and that I am able to determine tight limits on the abundance scatter in 15 elements, implies that the effects discussed in the previous paragraph must be small, at least for the red giants investigated here. This places strong limits on the probability and efficacy of the effects of rotation and binarity. From an operational viewpoint, this is good news for the prospect of performing detailed Galactic archaeology through large-scale chemical tagging. The old open clusters that we observe today most likely represent a population of stars where the effects of rotation and binarity would be the strongest, such that variations due to these confounding factors should be even smaller among field stars born in more loosely-bound associations. These variations would furthermore likely be largest for the surface abundances of C, N, and O (because they have large abundances, are strongly affected by mixing, and would be transferred by stellar winds to binary companions). These are the elements for which I obtain the strongest constraints, with intrinsic

scatter constrained to be < 0.025 dex at 95 % confidence in each of these. It does therefore not require a large leap of faith to assume that such limits are possible for all elements, especially in the light of the considerations in the next section. Thus, we should be able to determine the fine-grained structure of (initial) abundance space of the Milky Way, given a large enough sample of stars with high-resolution spectra.

Further development of the empirical technique presented in this paper should also allow chemical tagging to be performed in a manner that is less prone to systematics and that requires less input from stellar physics. That is, a promising way forward for chemical tagging is to search for one-dimensional sequences among a library of spectra, rather than searching for zero-dimensional loci in abundance space. Aside from being more robust against systematics, this will also allow C and N to be fully used for giants, because they are currently often excluded because of the effects of deep mixing (e.g., Ting et al. 2015). While a second-order-polynomial model suffices to describe the empirical stellar-mass trends of the red-giant spectra in the current sample, data sets that contain a wider variety of stellar types (including, for example, main-sequence stars and sub-giants) likely require more flexible one-dimensional models. This is especially the case when sharp changes in the surface abundances, e.g., due to the first dredge up (Iben 1964), occur within the sample.

6.2. The formation of star clusters

The tight constraints on the initial abundance scatter in open clusters places strong limits on how star formation in molecular clouds—the progenitors of open clusters—proceeds. This is especially the case because of the strong limits on the scatter in C, N, and O. C and O are produced in large quantities in core-collapse supernovae (CCSNe). Using the yields at solar metallicity from Chieffi & Limongi (2004) and Limongi & Chieffi (2006), we find that $\approx 0.9 M_{\odot}$ and $3.5 M_{\odot}$ of C is produced in a single CCSN of a $35 M_{\odot}$ and a $60 M_{\odot}$ star, respectively; for O the yield is even higher: $\approx 5 M_{\odot}$ and $8.5 M_{\odot}$ for the same two masses. Assuming that this amount of C or O is mixed in with $\approx 20,000 M_{\odot}$ of gas with solar abundance ratios from Asplund et al. (2005), subsequent stars would have C abundances higher by ≈ 0.02 dex and 0.04 dex and O abundances higher by ≈ 0.02 dex and 0.03 dex for a single CCSN of a $35 M_{\odot}$ and $60 M_{\odot}$ star. For comparison, the amount of Fe produced in these CCSNe is only about 0.1 to $0.2 M_{\odot}$ and raises the Fe abundances of new stars by ≈ 0.004 dex.

The fact that the initial scatter in C and O is constrained to be $\lesssim 0.025$ dex at 95 % confidence implies that no pollution by massive CCSNe occurred before most of the stars formed. The initial masses of M67 and NGC 6819 were likely in the range $10,000 M_{\odot}$ to $20,000 M_{\odot}$ (Hurley et al. 2005; Yang et al. 2013). Using the IMF from either Kroupa (2001) or Chabrier (2003), we would expect ≈ 11 and 5 stars with masses greater than $35 M_{\odot}$ and $60 M_{\odot}$, respectively, in a cluster with a mass of $20,000 M_{\odot}$. Thus, we would expect CCSNe of $35 M_{\odot}$ to $60 M_{\odot}$ stars to occur in M67 and NGC 6819 and potentially even higher mass CCSNe, which would lead to even larger abundance scatter. For star formation lasting for a time τ_{SF} , the lack of a CCSN when K

massive stars with lifetimes τ_{CCSN} are expected to form gives the following PDF for τ_{SF} (assuming a flat prior)

$$p(\tau_{\text{SF}}|\text{no CCSN}) \propto \begin{cases} 1 & \text{if } \tau_{\text{SF}} < \tau_{\text{CCSN}} \\ \left(\frac{\tau_{\text{CCSN}}}{\tau_{\text{SF}}}\right)^K & \text{otherwise.} \end{cases}$$

This converges to a flat distribution between zero and τ_{CCSN} for large K , because of the increasing probability that a massive star is formed at the onset of star formation and because we cannot distinguish τ_{SF} that are smaller than τ_{CCSN} . For 11 expected $35 M_{\odot}$ stars (with lifetimes $\tau_{\text{CCSN}} \approx 5.7$ Myr) as well as for 5 expected $60 M_{\odot}$ stars ($\tau_{\text{CCSN}} \approx 4$ Myr; Bressan et al. 2012), this gives an upper limit on τ_{SF} of ≈ 6 Myr at 95 % confidence. This limit would obviously weaken if massive stars preferentially form after low-mass stars—although this is not expected to be the case (McKee & Tan 2002) and they may even form the earliest (Maschberger et al. 2010)—or if a significant portion of the SNe ejecta are introduced into a warm ISM phase that is not immediately available for star formation (e.g., Matzner & McKee 2000, but see Pan et al. 2012).

The fact that I find no scatter in the abundances of light elements also directly demonstrates that the type of pollution that occurs in globular clusters does not happen for open clusters. Globular clusters display significant abundance scatter and anti-correlations in the abundances of light elements (C, N, O, Na, Mg, Al; Gratton et al. 2004), believed to stem from pollution of the intracluster medium by intermediate-mass asymptotic giant branch stars (e.g., Ventura et al. 2001), fast-rotating massive stars (Decressin et al. 2007), or massive binaries (de Mink et al. 2009). The abundance scatter in all of the light elements commonly studied in globular clusters is < 0.03 dex at 95 % confidence in the open clusters analyzed here (except for Na, for which the limit is slightly weaker).

That the initial abundance scatter in open clusters is as small as 0.01 to 0.02 dex as found here challenges our understanding of the structure of molecular clouds. To attain this level of homogeneity, the gas and dust in star-forming clouds has to be very well mixed (Feng & Krumholz 2014; Hopkins & Lee 2015) and, as argued above, star formation has to proceed within about 6 Myr. This is an important new constraint on the timescale of star formation in molecular clouds (e.g., Elmegreen 2000; Tan et al. 2006; Matzner 2007). The timescale constraint derived here is limited not by the constraint on the abundance spread, but instead by whether a CCSN of a massive star is likely to have occurred and to have polluted the star-forming gas. Therefore, the kind of limits derived here will not be able to be improved much further.

6.3. Final remarks

For many of the questions relating to the formation and evolution of star clusters and galactic disks that we

may answer using detailed measurements of stellar abundances, the *precision* in the abundances is of much higher importance than their overall accuracy. However, much of the modeling effort currently going into the analysis of large spectroscopic surveys is focused on improving the theoretical modeling of stellar photospheres (e.g., Magic et al. 2013) or line formation beyond the simplest models (e.g., Bergemann et al. 2012). While more realistic modeling of the stellar photospheres, radiative transfer, and line formation will provide a significant improvement for any spectroscopic analysis, it is unlikely that all systematic effects in the abundances will be removed through these efforts in the near future. This is especially the case for the effects of, e.g., deep mixing or atomic diffusion that actually change the surface abundances in a manner that is not entirely well understood (e.g., Önehag et al. 2014).

The method introduced here is wholly focused on obtaining the highest possible abundance precision given the observational limitations. It does this at the expense of some of the information in the spectra, which instead of being used to constrain the abundance scatter, is used to build an empirical model of the spectra. That the new technique leads to some of the tightest constraints on the intrinsic abundance scatter in open clusters and that it does this based on the complex infrared APOGEE spectra of giants that likely have intrinsic variations in C and N, is a testament to the strength of this new technique. I expect that extensions of this technique to other groupings of stars and to the whole Galactic disk population will lead to fundamentally new insights into the formation and evolution of stellar populations in the Milky Way.

It is with great pleasure that I thank the APOGEE ASPCAP team for many valuable discussions regarding infrared spectroscopy and APOGEE. In particular, I thank Carlos Allende Prieto, Katia Cunha, Anibal García-Hernández, Jon Holtzman, Szabolcs Mészáros, Matthew Shetrone, and Olga Zamora for help with the APOGEE ATLAS9 model atmospheres, *Turbospectrum* and *M00G*, the APOGEE line list, the APOGEE LSF, and the APOGEE pipeline. I further acknowledge insightful conversations with and comments from the anonymous referee, Ewan Cameron, David Hogg, Chris McKee, Melissa Ness, Garrett Somers, and Yuan-Sen Ting. I also thank the Natural Sciences and Engineering Research Council of Canada for financial support of this project.

Funding for SDSS-III has been provided by the Alfred P. Sloan Foundation, the Participating Institutions, the National Science Foundation, and the U.S. Department of Energy Office of Science. The SDSS-III web site is <http://www.sdss3.org/>.

APPENDIX

A. HIGH SIGNAL-TO-NOISE RATIO MEAN *H*-BAND SPECTRA FOR M67, NGC 6819, AND NGC 2420

In this appendix, I display the combined cluster spectra for M67, NGC 6819, and NGC 2420. These are obtained from the quadratic fits to each pixel using the modeling of § 2. Because the spectra of members of these clusters are all consistent with being a function of T_{eff} only, we can use the quadratic fit to their T_{eff} dependence to construct a very high signal-to-noise-ratio spectrum for each cluster. I compute the cluster spectrum at $T_{\text{eff}} = 4750$ K,

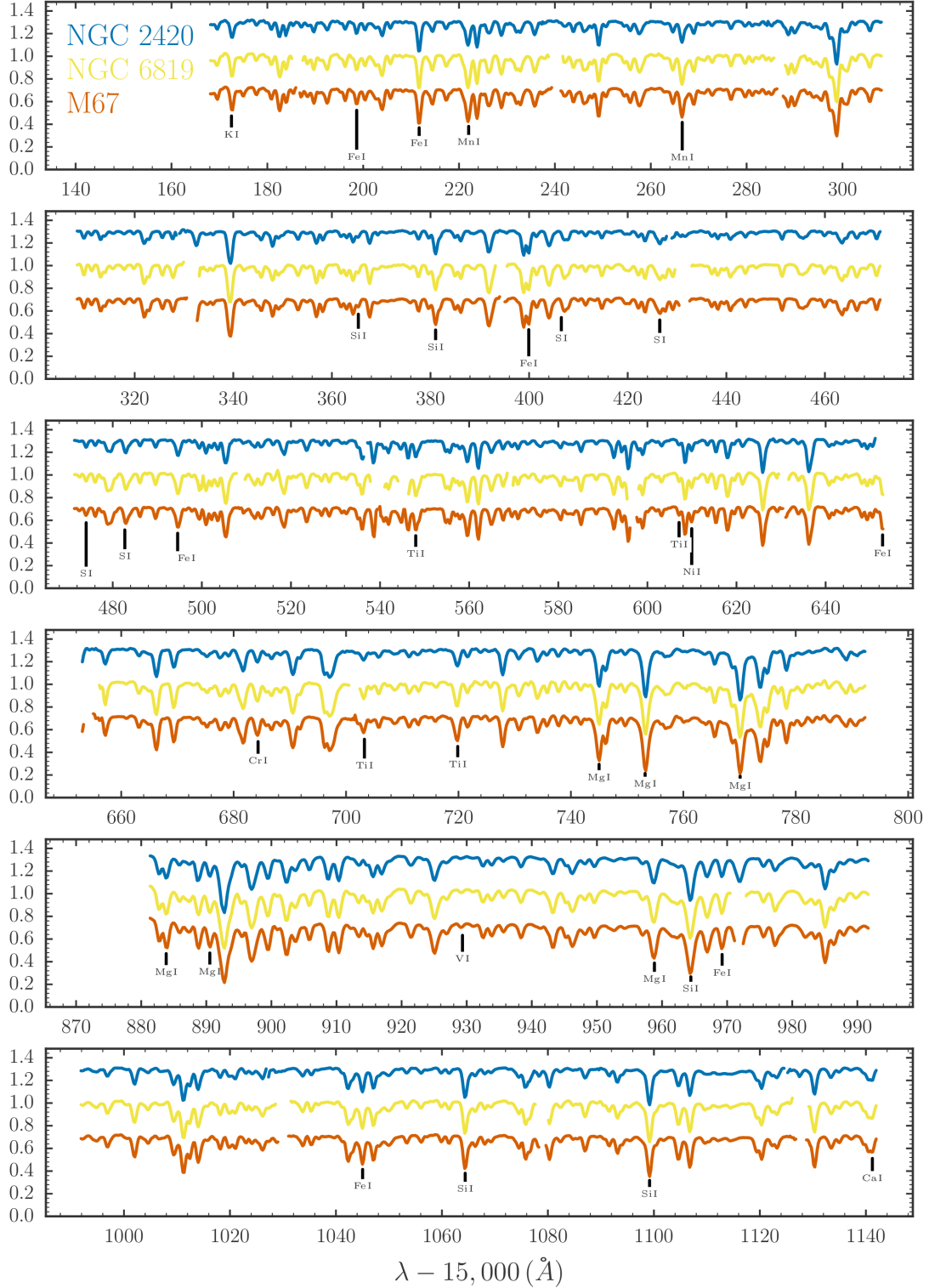


FIG. 9.— Combined continuum-normalized spectra between $\lambda \approx 15,150 \text{ \AA}$ and $16,150 \text{ \AA}$ for a first-ascent red giant at $T_{\text{eff}} = 4750 \text{ K}$ in M67, NGC 6819, and NGC 2420. These are determined from the quadratic fit to the T_{eff} dependence of each pixel using the red-giant members in each cluster (excluding red-clump stars). Strong, clean atomic lines from the compilation of Smith et al. (2013) for most of the elements considered in this paper (and some others) are indicated. The spectra for M67 and NGC 2420 are offset by -0.3 and 0.3 , respectively. Almost every feature, including weak ones, are reproduced in all three spectra, demonstrating that these spectra contain very little noise.

which is close to the median T_{eff} of all of the considered cluster members. To avoid any confusion due to the inclusion of red-clump stars in M67 and NGC 6819, I only include first-ascent red giants in the quadratic fit and the cluster

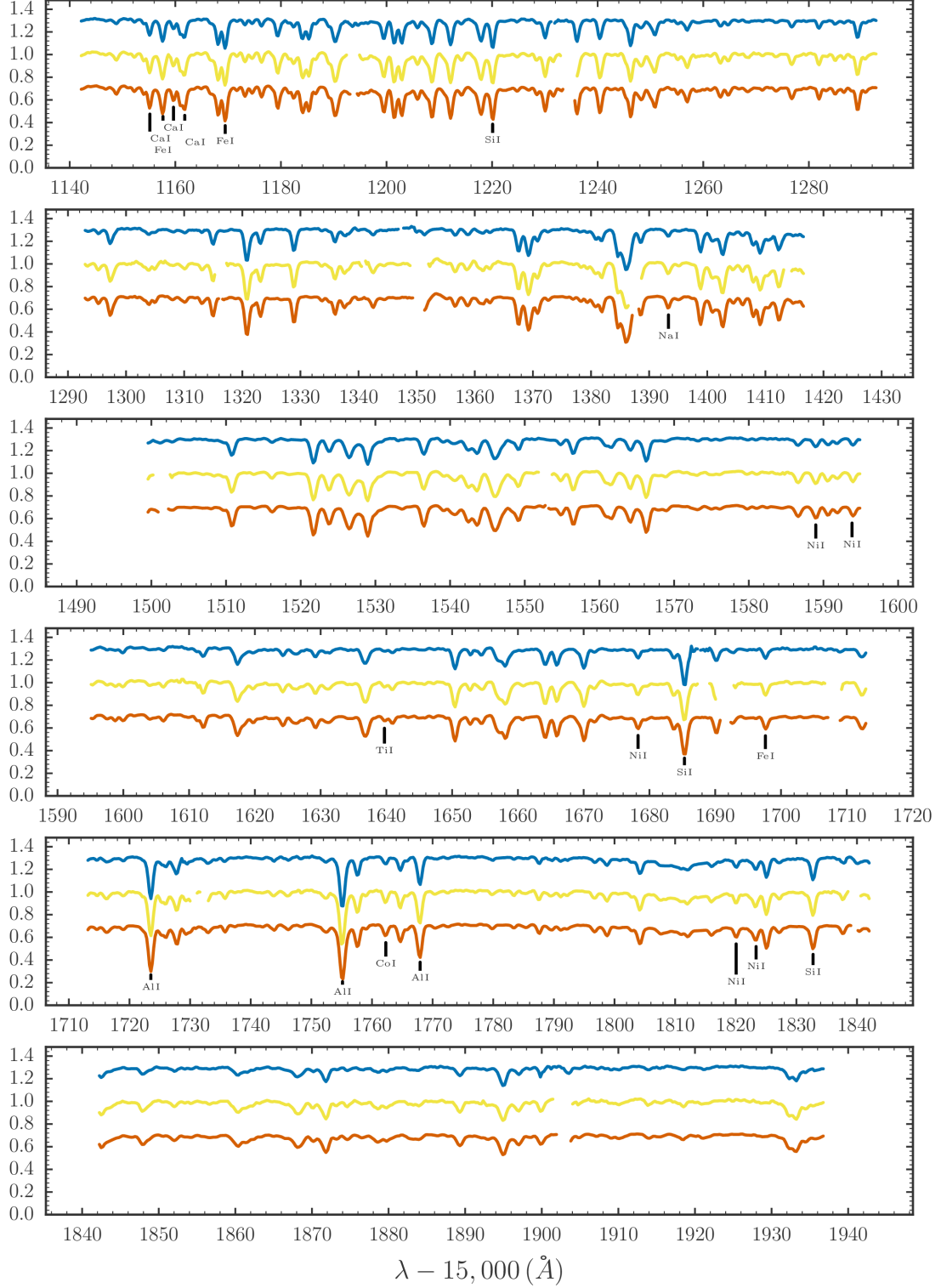


FIG. 10.— Same as Figure 9, but for the wavelength range $\lambda \approx 16,150 \text{ \AA}$ to $16,950 \text{ \AA}$.

spectrum is therefore that of a red giant in these clusters at $T_{\text{eff}} = 4750 \text{ K}$.

The cluster spectra are shown at high resolution in Figures 9 and 10. The three spectra are clearly very similar, especially those for M67 and NGC 6819 which are close in age and metallicity. Almost every single wiggle in the spectra is repeated in all three spectra, demonstrating the extremely high signal-to-noise ratio of these combined spectra. They could be used to obtain precise abundances for these clusters, but this is not done here as it is beyond the scope of this paper.

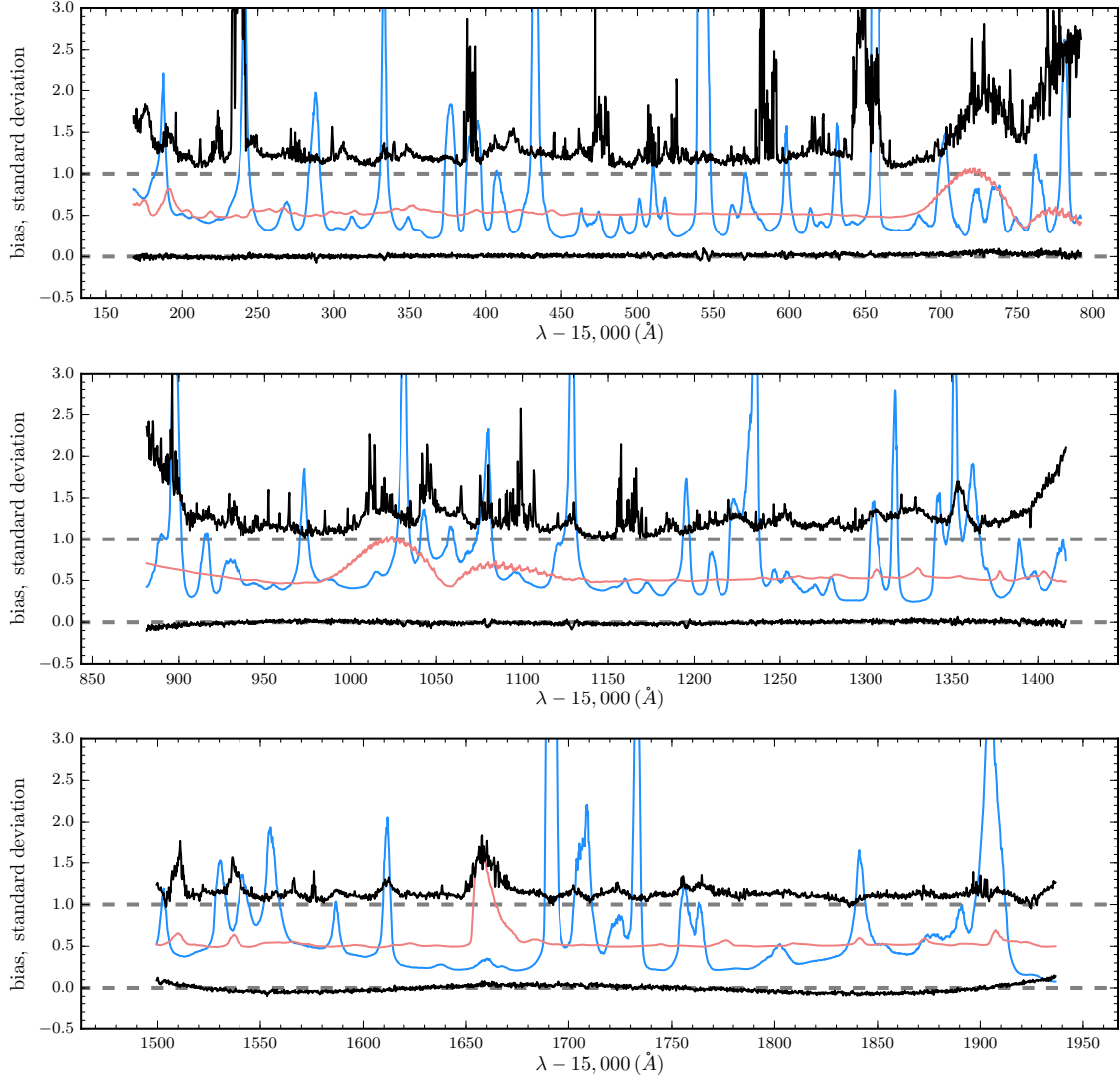


FIG. 11.— The median (bias; black line near zero) and standard deviation (black line above one) of the normalized residuals of individual exposures vs. combined continuum-normalized spectra of 1,381 stars with three exposures that individually have high signal-to-noise ratio. Each panel displays one of the three APOGEE detectors, which span three different wavelength ranges. The median is near zero, demonstrating that the continuum-normalized spectra are unbiased, with only minor effects due to the polynomial continuum-normalization. The standard deviation should be < 1 if the reported APOGEE spectral uncertainties were correct (see text), but is typically 1.1 to 1.2, with large wavelength regions where it is > 1.5 . The blue and red lines display the average sky and telluric spectra used to correct the individual spectra for the effect of sky-emission and telluric-absorption lines. Regions of high scatter in the residuals appear to largely coincide with those with significant telluric absorption.

B. EMPIRICAL INVESTIGATION OF THE APOGEE SPECTRAL ERRORS USING REPEAT OBSERVATIONS

As discussed in § 3, the APOGEE spectra have associated pixel-level uncertainties in the standard DR12 data products. These are obtained from a noise model that tracks the Poisson photon-counting noise through the APOGEE pipeline. These uncertainties are for single pixels only; correlations between the errors of neighboring pixels are not tracked. Nidever et al. (2015) tested these uncertainties using the scatter in the repeat observations of stars with six individual hour-long exposures, demonstrating that the uncertainties overall track the scatter well, but also finding a systematic error floor at the 0.5% level (see discussion in § 3). This test did not distinguish between pixels at different wavelengths and regions with significant sky-emission or telluric-absorption lines were avoided.

I perform a similar, but more detailed, test here and furthermore determine an empirical model for the spectral errors using repeat observations. I select giants from the APOGEE DR12 data set with $4000 \text{ K} \leq T_{\text{eff}} \leq 5000 \text{ K}$ and $\log g < 3.5$. Of these giants, I consider those with $10 < H < 11$ with three hour-long exposures that on average have an overall signal-to-noise ratio per half-resolution element larger than 100 (thus, their combined spectrum has signal-to-noise ratio larger than 300). These characteristics are similar to the majority of the open-cluster members considered in this paper. This sample consists of 1,381 stars with 3 repeat observations each for a total of 4,143 individual spectra. All of the individual spectra have an overall signal-to-noise ratio larger than 80.

I then continuum-normalize each individual-exposure spectrum as well as the combined APOGEE spectrum for each

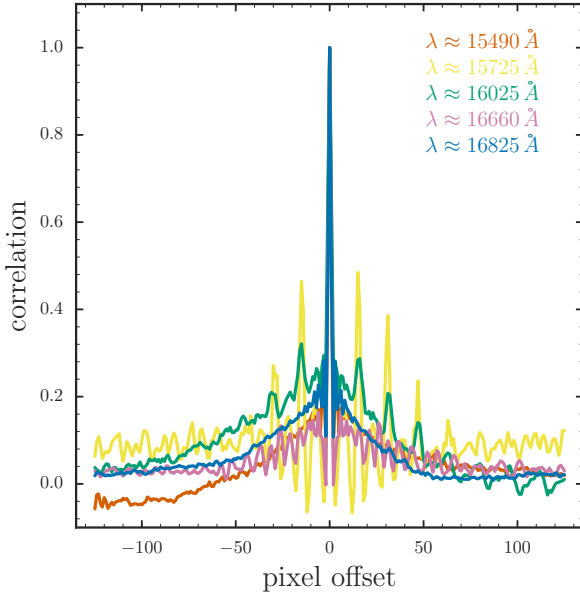


FIG. 12.— Correlations between the errors in neighboring pixels determined from repeat observations (see Figure 11) for five different central pixels. Significant correlations exist out to dozens of pixel offsets, both in regions of high and low scatter in the repeats (see Figure 11). This is much wider than the line-spread function and is most likely due to the continuum normalization.

of these stars in the manner described in § 3 and compute the normalized residuals

$$\Delta f_{\lambda}^i / \delta_{\lambda}^i = \frac{f_{\lambda}^i - f_{\lambda}^{i,\text{combined}}}{\delta_{\lambda}^i} \quad (\text{B1})$$

for each star i , where δ_{λ}^i is the pipeline uncertainty for each pixel λ . Pixels with signal-to-noise ratio less than 50 or with any of the bad pixel flags discussed in § 3 are removed from further consideration.

The median of the normalized residuals $\Delta f_{\lambda}^i / \delta_{\lambda}^i$ is displayed in Figure 11 and it measures the bias in the spectra taking into account the effects of continuum normalization. It is clear that the bias is small for all wavelengths, although minor polynomial trends especially in the green detector (middle panel) and the red detector (bottom panel) remain; these are due to the polynomial continuum fitting not being quite reproducible between different observations of the same star. I have also performed the same test using the standard APOGEE continuum-normalization method (García Pérez et al. 2015) and found significantly larger biases (up to about 0.5) that could negatively affect parameter and abundance determinations from these spectra. Similarly, I found larger biases when using only a second-order polynomial as in Ness et al. (2015).

The standard deviation of the normalized residuals is also shown in Figure 11 and is typically about 1.1 to 1.2, but with large wavelength ranges where the standard deviation is larger than 1.5. Because the three individual exposures are compared to their combined value, the distribution of the sum of the squares of the normalized residuals should follow a χ^2 distribution with two degrees of freedom if the pipeline uncertainties are correct and the standard deviation of all residuals should be approximately 2/3. Therefore, the fact that the standard deviation is larger than 2/3 demonstrates that the pipeline uncertainties are underestimated. Figure 11 also contains the median sky and telluric spectra that were used to correct the individual exposures used here. As expected because I remove any pixels near sky lines, the location of sky lines does not appear to be correlated with large values of the standard deviation of the residuals. However, these large values do appear to coincide with regions with significant telluric absorption. It is therefore likely that the underestimated uncertainties are due to issues with the telluric correction.

We can use the same normalized residuals to investigate the correlations between the errors of neighboring pixels. Figure 12 displays the correlation for five pixels chosen to represent a range of detectors and of regions with low and high scatter in the normalized residuals. This figure clearly demonstrates that there typically are significant correlations out to dozens of pixel offsets, corresponding to $\gtrsim 10 \text{ \AA}$. This is much wider than the wavelength region over which the line spread function is significant and these correlated errors are most likely due to correlations induced by the continuum normalization, although they may also have some contribution from scattered light.

When relating the differences in the spectra of stars to those expected from scatter in the abundances, it is essential to have a good understanding of the random errors and their correlations that affect these differences. Rather than using the repeat observations to build an empirical noise model incorporating the correlations between pixels, I directly use the normalized residuals determined from the repeat observations as an empirical sampling of the noise. This has the advantage of being incredibly straightforward. When looking at the residuals of the spectra in a given cluster from the one-dimensional model using the method of § 2 as applied in § 4, I simply compare to the distribution determined

from the repeat observations. Similarly, in the forward simulations described in § 5 and in Appendix C, I simply draw from the set of normalized residuals in the process of determining a mock error. However, because the residuals come from a comparison between an individual exposure and a combined spectrum that contains information from this individual exposure, the residuals are slightly smaller than the true error (because the three residuals for a given star only have two degrees of freedom). For the purposes of this paper, this is a conservative mistake, because it means that we are slightly underestimating the uncertainties in the spectra. This will slightly inflate any limit on the abundance scatter of the open clusters studied here. This could be fixed in the future by using the residuals determined from repeat observations to infer a noise model or it could be ameliorated by increasing the number of repeat exposures to $\gg 3$. Another problem is that if the underestimation of the pipeline uncertainties is truly due to the telluric-absorption correction, a model for the uncertainties in the Earth’s restframe rather than in the star’s restframe is necessary.

C. SYNTHETIC APOGEE SPECTRA

In §§ 4 and 5, I employ synthetic APOGEE spectra varying the abundances of 15 elements with absorption lines in the APOGEE wavelength range. This Appendix explains how I generate these synthetic spectra. For each individual star, I generate a model atmosphere at the median metallicity of the cluster and at the $(T_{\text{eff}}, \log g)$ of the star, using solar abundance ratios for all elements. The model atmosphere is obtained using linear interpolation of the grid of atmospheres computed using the ATLAS9 code by Mészáros et al. (2012). These atmospheres and the synthetic spectra computed using them all use the solar abundances from Asplund et al. (2005). I compute synthetic spectra varying the abundances of individual elements using *Turbospectrum* (Alvarez & Plez 1998), adopting the microturbulence prescription as a function of $\log g$ used in APOGEE DR12, an isotopic ratio $C^{12}/C^{13} = 15$ appropriate for giants, and using a Gaussian macroturbulence with a full-width-at-half-maximum of 6 km s^{-1} . This macroturbulence is at the high end of what is expected for the giants in this sample, but oversmoothing the spectrum is conservative in that it would weaken any result on abundance variations from spectral scatter. I employ the same line list as used in APOGEE’s DR12 (Shetrone et al. 2015), with astrophysical *gfs* determined by fitting the *H*-band spectra of the Sun and Arcturus, but fitting to the center-of-disk solar flux (M. Shetrone, private communication), i.e., with the total-flux vs. center-of-disk bug in the APOGEE DR12 line list fixed (see Shetrone et al. 2015). Synthetic spectra are computed in air wavelengths over the wavelength range 15,000 to 17,000 Å with a wavelength step of 0.05 Å.

Each of the 300 APOGEE fibers has a different LSF. Variations in the width of the LSF between different fibers are typically 10 to 20 %, but the LSF of individual fibers are stable at the 1 % level (Nidever et al. 2015). The APOGEE LSF is non-Gaussian and detailed forward modeling of the spectra needs to take the non-Gaussian, variable nature of the LSF into account. I compute the LSF of each fiber using the Gauss-Hermite-expansion fit to the LSF of each fiber (which additionally includes a wide Gaussian for the wings of the LSF) and the wavelength calibrations for all three detectors, which are publicly available (Nidever et al. 2015). For each cluster star I average the LSFs of the fibers used for the hour-long individual exposures. The raw synthetic spectra from *Turbospectrum* are interpolated onto a wavelength grid in vacuum wavelengths using the transformations from Ciddor (1996). They are then convolved with the LSF and brought onto the same wavelength grid as the observed spectra. These spectra are then continuum-normalized using the procedure described in § 3.

To add errors to the continuum-normalized synthetic spectra, I draw from the set of 4,143 normalized residuals from repeat observations (see Appendix B). This normalized error is then “de-normalized” by multiplying it with the uncertainty array of the observed spectrum and the result is added to the synthetic spectrum. Any bad pixels in the observed spectrum of a cluster star are also labeled as bad in the synthetic spectra for that star. In drawing from the normalized residuals, only those residuals with a smaller number of bad pixels than the observed spectrum are used. In generating synthetic spectra for changes in different elements, this number of bad pixels is computed by weighting with the sensitivity weights for each element that are discussed in Appendix D. That is, only bad pixels in the spectral regions with absorption features for the given element are taken into account. This procedure creates synthetic spectra that are very similar to the observed spectra in LSF, errors, and distribution of bad pixels.

All of the code to generate these synthetic spectra is available online as part of a general-use APOGEE data-analysis Python package called *apogee*, available at

<http://github.com/jobovy/apogee>.

This package allows one to download and open the necessary data files containing the APOGEE catalog and spectra. Tools for reading the ATLAS9 APOGEE model atmosphere grid², interpolating within the grid using linear interpolation, and outputting the model atmospheres in a format suitable for MOOG (Snedden 1973) or *Turbospectrum* are included in *apogee.modelatm*. Synthetic spectra can be calculated using MOOG or *Turbospectrum* with a similar Python interface using functions in *apogee.modelspec.moog* and *apogee.modelspec.turbospec*. These include functions to simply compute the high-resolution theoretical spectra or to generate full synthetic spectra including LSF and macroturbulence convolution, re-sampling onto the observed wavelength grid, and continuum normalization.

Tools for computing the LSF and convolving with it efficiently using sparse-matrix algebra are contained in *apogee.spec.lsf*. Continuum-normalization using the standard APOGEE method (García Pérez et al. 2015) or the method of Ness et al. (2015) (as used in this paper) are implemented in *apogee.spec.cont*. Various tools for handling the sensitivity windows described in Appendix D are included in *apogee.spec.windows*. The code to fit a linear or quadratic model in stellar labels (T_{eff} in this paper, see § 2 and Ness et al. 2015) is included in

² Available here: <http://www.iac.es/proyecto/ATLAS-APOGEE/>.

TABLE 3
SPECTRAL VARIATIONS FOR 0.1 DEX ABUNDANCE CHANGES

Window	C	N	O	Na	Mg	Al	Si	S	K	Ca	Ti	V	Mn	Fe	Ni
C	0.022	30	31	1	17	2	8	1	9	1	0	1	1	30	2
N	113	0.013	65	1	23	4	12	1	0	2	0	0	0	23	2
O	123	82	0.007	2	40	46	17	3	0	6	8	1	3	118	11
Na	29	21	20	0.010	5	0	3	0	0	0	1	0	0	12	2
Mg	9	5	3	0	0.030	1	5	0	0	0	0	1	1	34	0
Al	16	11	7	0	10	0.025	7	0	0	1	0	0	0	14	1
Si	12	7	6	0	12	1	0.023	0	0	1	2	0	0	17	1
S	19	13	21	0	13	1	4	0.015	0	1	0	0	0	14	1
K	58	45	36	1	12	1	6	0	0.026	1	0	0	2	12	1
Ca	13	6	1	0	3	0	4	0	0	0.027	1	0	0	34	0
Ti	7	9	12	0	3	0	2	0	0	0	0.015	0	0	12	1
V	36	27	23	2	4	1	11	0	0	3	1	0.011	2	30	1
Mn	3	4	23	0	5	1	3	0	0	0	0	0	0.029	5	2
Fe	12	9	8	0	8	1	7	1	0	1	6	0	1	0.027	2
Ni	22	7	8	0	10	1	6	1	0	1	0	0	0	46	0.019

NOTE. — This table gives the changes in the spectrum of a $T_{\text{eff}} = 4750$ K, $\log g = 2.5$ star with solar abundances due to abundance changes of ± 0.1 dex for the 15 elements considered in this paper. Each row weights the spectral changes due to each individual element using the weights for this row’s element that I derived from the standard APOGEE weights in Appendix D. Thus, the first line uses the weights for C to compute the weighted spectral variations due to different elements. The diagonal gives the actual weighted variation in the continuum-normalized spectrum, while the off-diagonal entries list the changes as a percentage of the diagonal entry. For example, N induces changes that are 34% of those induced by the same change in C when weighting using C weights. Using the set of weights from Appendix D, the weighted spectral regions for all elements except for C, N, and O have only minor contributions from other elements.

apogee.spec.cannon. Aside from these tools used in the analysis in this paper, the **apogee** package also contains a full implementation of the standard APOGEE stellar-parameters and elemental-abundances pipeline using **FERRE**³. This is included in **apogee.modelspec.ferre**, which allows for interpolation of model spectra from the standard APOGEE grids (Zamora et al. 2015) and for performing the APOGEE stellar-parameter and abundance fits for any APOGEE spectrum.

D. SENSITIVITY OF APOGEE SPECTRA TO ABUNDANCE VARIATIONS OF DIFFERENT ELEMENTS

APOGEE’s abundance pipeline uses a set of numbers as a function of wavelength for each element to weight the contribution of different pixels to the $\Delta\chi^2$ when fitting for the abundance of that element. These numbers give high weight to pixels that are highly sensitive to the abundance of the element in question and not that sensitive to the abundance of other elements. They are computed from the derivatives of model spectra at $T_{\text{eff}} = 4000$ K, $\log g = 1$, and overall metallicity of -2.0 , -1.0 , and 0.0 and they also take into account how well a model for the spectrum of Arcturus reproduces the high resolution, high signal-to-noise ratio observed spectrum of Arcturus of Hinkle et al. (1995), how well the whole APOGEE sample is fit at each pixel, and how well the stars analyzed in detail by Smith et al. (2013) are modeled. Full details on this procedure are given in García Pérez et al. (2015).

In this paper, I make use of these weights (also referred to as “windows”) to analyze the spectral variations induced by abundance changes of different elements. That is, when determining, for example, the impact of Al variations, the APOGEE weights are used to only consider wavelengths that are sensitive to the Al abundance. This appendix describes some further analysis of the sensitivity of the standard APOGEE DR12 windows to changes in the abundances of different elements. The main purposes of this analysis are to specifically focus on abundance changes near solar metallicity and to create a subset of the standard windows that is less sensitive to the abundances of other elements, in particular C and N.

To do this, I compute a baseline synthetic APOGEE spectrum using the procedure described in Appendix C for a star with $T_{\text{eff}} = 4750$ K, $\log g = 2.5$, solar abundances, microturbulence of 2 km s^{-1} , and convolving with the average LSF of all APOGEE fibers. I then compute a set of spectra that vary the abundances of all 15 elements considered in this paper separately by ± 0.1 dex. The variations around the baseline spectrum are displayed for a few example elements in Figure 13. I then compute the root-mean-square deviation for this ± 0.1 dex change in all elements for each element’s windows, weighting by the APOGEE weights. For example, for Al I use the Al weights and then compute the root-mean-square variation in the spectrum for all 15 elements. This then returns the effect of each individual element’s abundance changes on the spectrum near the Al absorption features. In Figure 13, the element whose windows we are interested in is always displayed in blue and other elements are ranked by the relative contribution to the spectral scatter near the absorption features of that element.

Figure 13 demonstrates that the standard APOGEE weights for a given element (e.g., Mg) include many wavelength ranges with significant contributions from other elements (e.g., the two reddest Mg windows). To clean the list of windows for each element, I compute the variation induced by other elements for each individual window for that element (roughly, an individual absorption feature, but for this can be quite extended for the molecular features). For example, for each of the two Al windows in Figure 13, I compute the variation induced by Al and all other elements. I

³ <http://www.as.utexas.edu/~hebe/ferre/>.

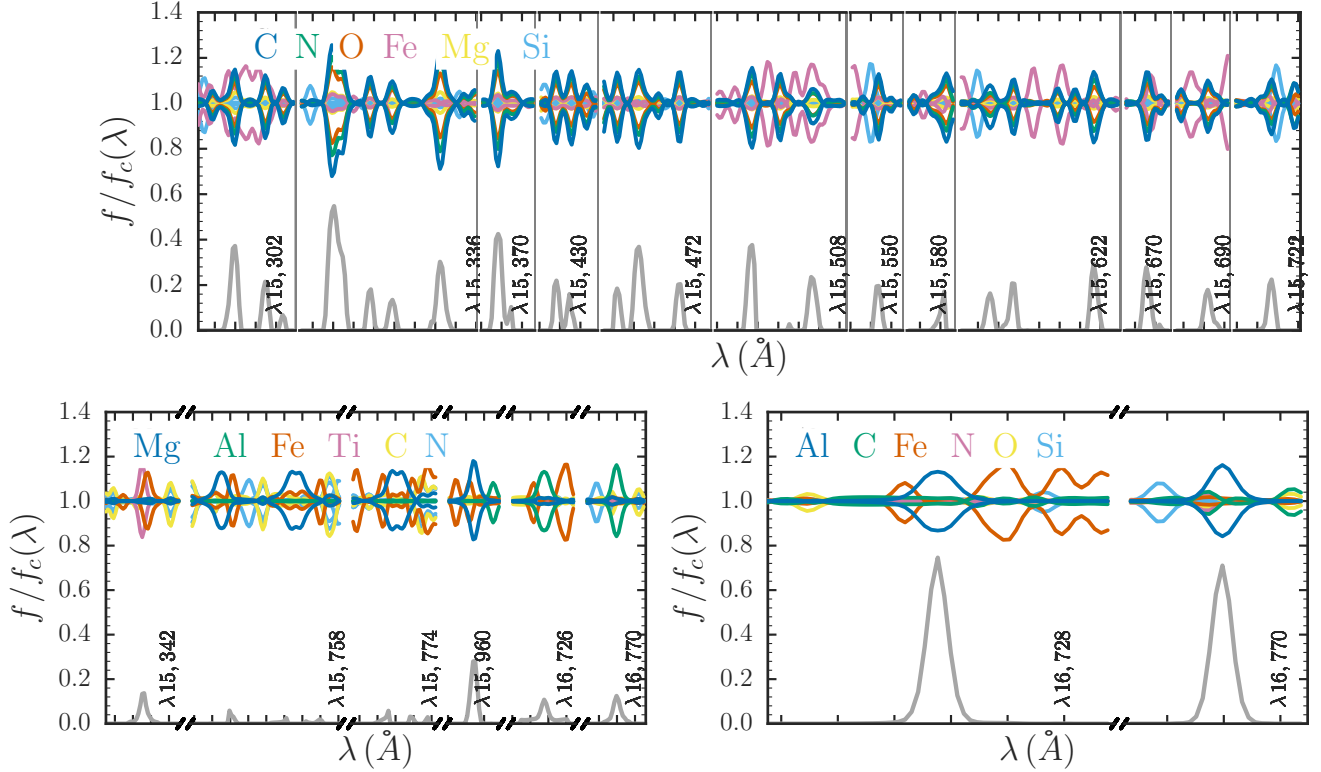


FIG. 13.— Variations in the spectrum of a $T_{\text{eff}} = 4750$ K, $\log g = 2.5$ star with solar abundances induced by ± 0.1 dex changes in the abundance of different elements. As examples, this figure shows those spectral variations in regions of the spectrum with C (top panel), Mg (bottom left panel), and Al (bottom right panel) absorption features; all variations are exaggerated by a factor of ten. The whole H -band wavelength range is broken into small regions and the separation in x tickmarks is always 2 \AA ; the wavelength of a single tickmark in each region is indicated. Variations due to elements other than C in the top panels and other than Mg or Al in the bottom panels are ordered by their weighted root-mean-square variation, computed using the standard APOGEE weights for C, Mg, and Al, respectively. These weights are displayed as the gray lines. Only half of the features for C are displayed here. C has ubiquitous absorption features, but disentangling them from those of N and O is difficult. Some of the Mg APOGEE weights cover wavelength regions where Mg does not have absorption features (such as the two reddest regions) and I remove these from consideration here.

then remove any window that produces less than a 0.01 change in the continuum-normalized spectrum when varying the abundance of that window's element by ± 0.1 dex or if any of the other elements induce a variation greater than 34% of that induced by the window's corresponding element. For example, if the variation due to Al in the first Al window is 0.005, the window would be removed (this is not the case). Or if another element, say Mg, creates a spectral variation larger than 34% of that of Al in this window, the window would be removed (also not the case). Many of the elements require some fine tuning of these cuts to not remove too many individual windows: K is kept, because there is only a single line in the spectrum, other elements are allowed to contribute up to 100% or 200% for C and N, respectively (basically, because of the ubiquitous CN features), O is kept down to changes as small as 0.005 and up to contributions of other elements of 500% (because most O features are weak). Additionally, for Na, Ti, V, Mn, and Ni I only consider the contribution of other elements and use a cut-off of 34%, 30%, 40%, 25%, and 50%, respectively. While these cuts are somewhat arbitrary, they have been chosen to keep a reasonable number of windows for each element that are not too affected by variations in other elements.

The weighted variations induced in the spectrum by ± 0.1 dex abundance changes for the final set of weights are given in Table 3. Along the diagonal, this table gives the magnitude of spectral changes for each element weighted by the weights for that element. The off-diagonal entries show how much variation abundances changes in other elements induce, given as a percentage of the main element's variation. This demonstrates that we end up with a relatively clean set of weights for each element. Most ± 0.1 dex abundance changes induce weighted spectral variations of about 0.01 to 0.025, which is larger than the typical noise of each pixel. This weighted spectral variation, however, does not show the number of pixels at which such large variations exist. Elements with a large number of pixels with non-zero weights will lead to stronger constraints on abundance variations.

REFERENCES

- Alam, S., Albareti, F. D., Allende Prieto, C., et al. 2015, *ApJS*, 219, 12
- Alvarez, R. & Plez, B. 1998, *A&A*, 330, 1109
- Asplund, M., Grevesse, N., & Sauval, A. J. 2005, in *ASP Conf. Ser. 336, Cosmic Abundances as Records of Stellar Evolution and Nucleosynthesis*, ed. T. G. Barnes, III & F. N. Bash (San Francisco, CA: ASP), 25

- Bergemann, M., Lind, K., Collet, R., Magic, Z., & Asplund, M. 2012, *MNRAS*, 427, 27
- Blanco-Cuaresma, S., Soubiran, C., Heiter, U., et al. 2015, *A&A*, 577, A47
- Bland-Hawthorn, J., Krumholz, M. R., & Freeman, K. 2010, *ApJ*, 713, 166
- Bressan, A., Marigo, P., Girardi, L., et al. 2012, *MNRAS*, 427, 127
- Carlberg, J. K., Smith, V. V., Cunha, K., et al. 2015, *ApJ*, 802, 7
- Chabrier, G. 2003, *PASP*, 115, 763
- Chieffi, A. & Limongi, M. 2004, *ApJ*, 608, 405
- Ciddor, P. E. 1996, *Appl. Opt.*, 35, 1566
- Decressin, T., Meynet, G., Charbonnel, C., Prantzos, N., & Ekström, S. 2007, *A&A*, 464, 1029
- de Mink, S. E., Pols, O. R., Langer, N., & Izzard, R. G. 2009, *A&A*, 507, L1
- De Silva, G. M., Sneden, C., Paulson, D. B., et al. 2006, *AJ*, 131, 455
- De Silva, G. M., Freeman, K. C., Bland-Hawthorn, J., Asplund, M., & Bessell, M. S. 2007, *AJ*, 133, 694
- De Silva, G. M., Freeman, K. C., Asplund, M., et al. 2007, *AJ*, 133, 1161
- Elmegreen, B. G. 2000, *ApJ*, 530, 277
- Feng, Y. & Krumholz, M. R. 2014, *Nature*, 513, 523
- Freeman, K. & Bland-Hawthorn, J. 2002, *ARA&A*, 40, 487
- García Pérez, A. E., Allende Prieto, C., Holtzman, J. A., et al. 2015, *AJ*, submitted
- Gilroy, K. K. & Brown, J. A. 1991, *ApJ*, 371, 578
- Gratton, R., Sneden, C., & Carretta, E. 2004, *ARA&A*, 42, 385
- Gunn, J. E., Siegmund, W. A., Mannery, E. J. et al. 2006, *AJ*, 131, 2332
- Hinkle, K., Wallace, L., & Livingston, W. 1995, *PASP*, 107, 1042
- Holtzman, J. A., Shetrone, M., Johnson, J. A., et al. 2015, *AJ*, 150, 148
- Hopkins, P. F. & Lee, H. 2015, *MNRAS*, in press (arXiv:1510.02477)
- Hurley, J. R., Pols, O. R., Aarseth, S. J., & Tout, C. A. 2005, *MNRAS*, 363, 293
- Iben, I., Jr. 1964, *ApJ*, 140, 1631
- Kawaler, S. D. 1988, *ApJ*, 333, 236
- Kroupa, P. 2001, *MNRAS*, 322, 231
- Lada, C. J. & Lada, E. A. 2003, *ARA&A*, 41, 57
- Limongi, M. & Chieffi, A. 2006, *ApJ*, 647, 483
- Magic, Z., Collet, R., Asplund, M., et al. 2013, *A&A*, 557, A26
- Majewski, S. R., Schiavon, R. P., Frinchaboy, P. M., et al. 2015, *AJ*, submitted (arXiv:1509.05420)
- Marin, J.-M., Pudlo, P., Robert, C. P., & Ryder, R. J. 2012, *Stat. Comput.*, 22, 1167
- Maschberger, T., Clarke, C. J., Bonnell, I. A., & Kroupa, P. 2010, *MNRAS*, 404, 1061
- Matzner, C. D. & McKee, C. F. 2000, *ApJ*, 545, 364
- Matzner, C. D. 2007, *ApJ*, 659, 1394
- McKee, C. F. & Tan, J. C. 2002, *Nature*, 416, 59
- Meléndez, J., Asplund, M., Gustafsson, B., & Yong, D. 2009, *ApJ*, 704, L66
- Mészáros, S., Allende Prieto, C., Edvardsson, B., et al. 2012, *AJ*, 144, 120
- Mészáros, S., Holtzman, J., García Pérez, A. E., et al. 2013, *AJ*, 146, 133
- Mészáros, S., Martell, S. L., Shetrone, M., et al. 2015, *AJ*, 149, 153
- Meynet, G. & Maeder, A. 2002, *A&A*, 390, 561
- Ness, M., Hogg, D. W., Rix, H.-W., Ho, A. Y. Q., & Zasowski, G. 2015, *ApJ*, 808, 16
- Nidever, D. L., Holtzman, J. A., Allende Prieto, C., et al. 2015, *AJ*, 150, 173
- Önehag, A., Gustafsson, B., & Korn, A. 2014, *A&A*, 562, A102
- Pan, L., Desch, S. J., Scannapieco, E., & Timmes, F. X. 2012, *ApJ*, 756, 102
- Pinsonneault, M. H., Kawaler, S. D., & Demarque, P. 1990, *ApJS*, 74, 501
- Pritchard, J. K., Seielstad, M. T., Perez-Lezaun, A., & Feldman, M. W. 1999, *Mol. Biol. Evol.*, 16, 1791
- Reddy, A. B. S., Giridhar, S., & Lambert, D. L. 2012, *MNRAS*, 419, 1350
- Shetrone, M., Bizyaev, D., Lawler, J. E., et al. 2015, *ApJS*, 221, 24
- Shu, F. H., Adams, F. C., & Lizano, S. 1987, *ARA&A*, 25, 23
- Skumanich, A. 1972, *ApJ*, 171, 565
- Smith, V. V., Cunha, K., Shetrone, M. D., et al. 2013, *ApJ*, 765, 16
- Sneden, C. A. 1973, PhD thesis, Univ. Texas, Austin
- Tan, J. C., Krumholz, M. R., & McKee, C. F. 2006, *ApJ*, 641, L121
- Tavaré, S., Balding, D. J., Griffith, R. C., & Donnelly, P. 1997, *Genetics*, 145, 505
- Ting, Y.-S., De Silva, G. M., Freeman, K. C., & Parker, S. J. 2012, *MNRAS*, 427, 882
- Ting, Y.-S., Conroy, C., & Rix, H.-W. 2015, *ApJ*, in press (arXiv:1507.07563)
- Ventura, P., D’Antona, F., Mazzitelli, I., & Gratton, R. 2001, *ApJ*, 550, L65
- Weber, E. J. & Davis, L., Jr. 1967, *ApJ*, 148, 217
- Wilson, J. C., Hearty, F., Skrutskie, M. F., et al. 2010, *Proc. SPIE*, 7735, 46
- Yang, S.-C., Sarajedini, A., Deliyannis, C. P., et al. 2013, *ApJ*, 762, 3
- Zamora, O., García-Hernández, D. A., Allende Prieto, C., et al. 2015, *AJ*, 149, 181
- Zasowski, G., Johnson, J. A., Frinchaboy, P. M., et al. 2013, *AJ*, 146, 81